nature COMMUNICATIONS

ARTICLE

Received 24 Oct 2013 | Accepted 24 Jun 2014 | Published 24 Jul 2014

DOI: 10.1038/ncomms5494 OPEN

Retrieving the intracellular topology from multi-scale protein mobility mapping in living cells

Michael Baum[1], Fabian Erdel[1], Malte Wachsmuth[2] & Karsten Rippe[1]

In living cells, most proteins diffuse over distances of micrometres within seconds. Protein translocation is constrained due to the cellular organization into subcompartments that impose diffusion barriers and guide enzymatic activities to their targets. Here, we introduce an approach to retrieve structural features from the scale-dependent mobility of green fluorescent protein monomer and multimers in human cells. We measure protein transport simultaneously between hundreds of positions by multi-scale fluorescence cross-correlation spectroscopy using a line-illuminating confocal microscope. From these data we derive a quantitative model of the intracellular architecture that resembles a random obstacle network for diffusing proteins. This topology partitions the cellular content and increases the dwell time of proteins in their local environment. The accessibility of obstacle surfaces depends on protein size. Our method links multi-scale mobility measurements with a quantitative description of intracellular structure that can be applied to evaluate how drug-induced perturbations affect protein transport and interactions.

[1] Deutsches Krebsforschungszentrum (DKFZ) and BioQuant, Research Group Genome Organization and Function, Im Neuenheimer Feld 280, 69120 Heidelberg, Germany. [2] European Molecular Biology Laboratory, Cell Biology and Biophysics Unit, Meyerhofstr. 1, 69117 Heidelberg, Germany. Correspondence and requests for materials should be addressed to F.E. (email: F.Erdel@dkfz.de) or to K.R. (email: Karsten.Rippe@dkfz.de).

Cellular structures such as membranes, chromatin, cytoskeleton and cytoplasmic organelles form a dynamic three-dimensional maze through which proteins have to find their way to reach the sites where they are active. The topology of the cellular interior is a key factor for target search processes and enzymatic reactions[1] that are the basis for cell function. To map the properties of dynamic structures like chromatin in living cells as they are 'sensed' by a diffusing protein, direct visualization of all cellular constituents at high spatial and temporal resolution is needed. Currently, cryo-electron microscopy enables three-dimensional imaging of cellular structures at molecular resolution[2] but has the drawback that it is only applicable to fixed samples. Recent advances in super-resolution light microscopy allow for mapping labelled structures in living cells with sub-diffraction resolution of ~20 nm (ref. 3). However, they do not provide the temporal resolution required to follow fast molecular translocations. A complementary approach that is well established in the field of diffusion NMR is it to infer structural information from the mobility of an inert nanosensor that explores the accessible space of a structure[4–7]. This strategy has been successfully applied to investigate pore sizes and connectivity in rocks, clays and biological tissues[4,7,8]. Here, we introduce this concept to fluorescence correlation spectroscopy (FCS) to link protein mobility and cellular structure in single cells at high resolution[9–11]. To this end, we map the mobility of inert monomers, trimers and pentamers of the green fluorescent protein (GFP) domain on multiple length and time scales in the cytoplasm and nucleus by parallelized FCS measurements with a line-illuminating multi-focus fluorescence microscope. With drugs specifically targeting different cellular components we investigate how perturbations of the cellular structure affect protein transport. Furthermore, we compare the mobility of inert GFP multimers to GFP fusions of the signal transducer and activator of transcription 2 (STAT2) protein and the chromodomain of heterochromatin protein 1 beta (HP1β). From the perspective of these proteins that cover the size range of most enzymes, the cellular interior appears as a porous medium made up by randomly distributed obstacles with characteristic size and density. Its structure reorganizes in response to intra- and extracellular cues and acts as a viscous medium on large molecules, while it partitions the cellular content for smaller molecules.

Results

Protein mobility maps mirror the intracellular architecture. Cellular structures reduce molecular mobility in a time- and length-scale-dependent manner. Thus, mobility maps acquired on multiple scales contain hidden information on the cellular environment. To be able to simultaneously measure protein translocations with microsecond time resolution on multiple length scales from 0.2 to ~3 μm, we extended the principle of FCS measurements at a single point in the sample to simultaneous FCS measurements at hundreds of positions arranged along a line. For this purpose, we used a line-illuminating confocal microscope with parallel fluorescence signal acquisition from several hundred detection volumes positioned within the cell, where each detection volume corresponds to a pixel of an electron multiplying charge-coupled device (EM-CCD) detector array (Fig. 1a). This setup was previously introduced as a spatial and temporal fluctuation microscope (STFM)[12] and was further developed for the applications described here. When operated in the conventional FCS mode, fluorescence intensity fluctuations at each pixel can be evaluated with an auto-correlation (AC) analysis to obtain spatially resolved mobility and concentration

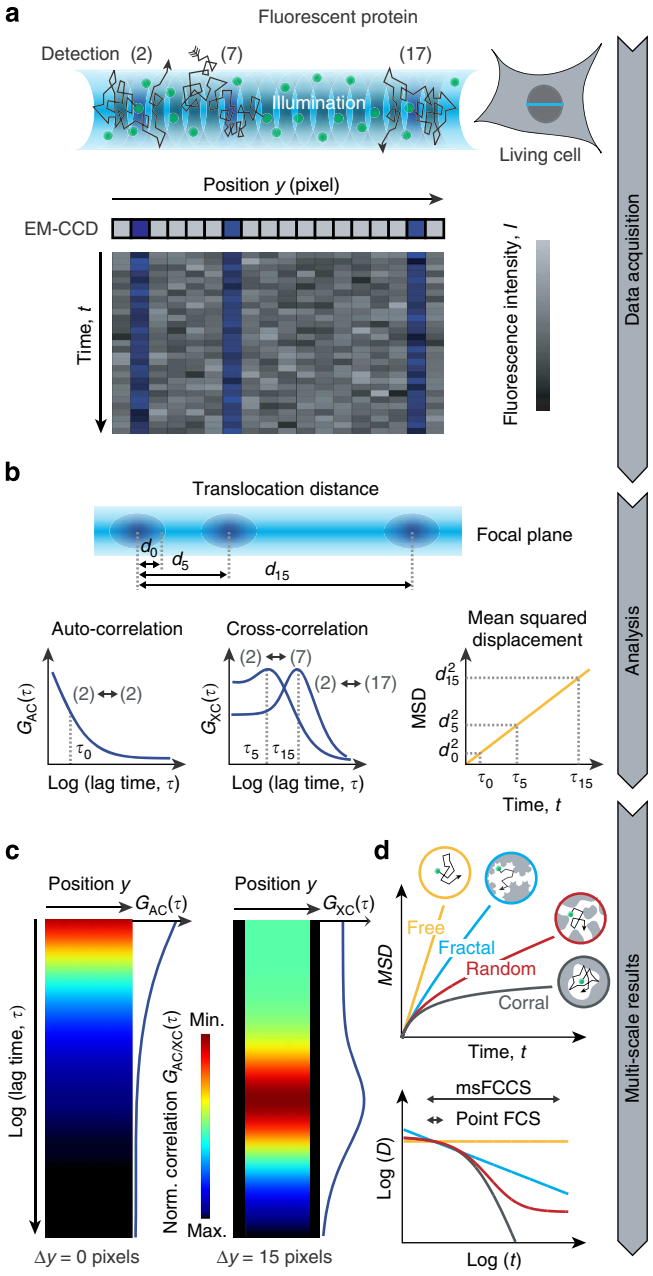

Figure 1 | Parallelized acquisition of fluorescence signals for msFCCS analysis. (**a**) Line illumination and parallelized multifocal fluorescence signal detection. Fluorescent proteins enter and leave the detection volumes by diffusion. The resulting local fluctuations in the fluorescence signal are detected on corresponding pixels of an EM-CCD camera array. (**b**) AC and XC analysis. By applying correlation analysis to the fluorescence signal recorded at a given detector pixel, AC curves can be calculated at every pixel position. Correlation of signals from spatially separated detection volumes are evaluated by computing XC curves (for example, signals of detection volumes 2 and 7 or detection volumes 2 and 17). These yield the MSD, the diffusion coefficient D and the concentration or molecule transmission rate as a function of the translocation distance d_n or translocation time τ_n. (**c**) AC curves or XC curves for a constant distance between detection elements are acquired along the illumination line and are visualized in so-called correlation carpets, from which diffusion barriers can be identified. (**d**) The diffusion coefficients determined for different distances can be used to reconstruct the molecules' MSD as a function of the diffusion time t. The time dependence of the diffusion coefficient reflects the nanostructure 'seen' by the diffusing protein. Norm, normalized.

profiles. In addition to parallelized AC measurements, the simultaneously recorded fluorescence signals can be used for fluorescence cross-correlation spectroscopy (FCCS) experiments: Cross-correlation (XC) analysis of signals from different detection volumes yields the diffusion coefficients for transport between selected positions along the line in living cells. Since this can be done for all combinations of the detection elements at the same time, thousands of XC functions can be obtained in a single experiment. For each distance between detection volumes, the diffusion coefficient is determined on the corresponding length and time scale. Simultaneous measurement of the diffusion coefficient on multiple scales allows for reconstructing the environment in which the transport process under study takes place (Fig. 1b). The approach described here to conduct this type of analysis is referred to as multi-scale FCCS (msFCCS). The resulting set of AC and XC curves obtained by msFCCS can be visualized as correlation carpets (Fig. 1c): Each column of the carpet represents a color-coded correlation curve as shown for idealized AC and XC carpets in homogeneous solution. AC carpets are simply the AC functions 'attached' vertically to each pixel along the horizontal axis that represents the detection line. XC carpets are obtained by computing XC curves for each pixel correlated with another pixel that is separated along the line by a fixed distance. The resulting XC curves are then assigned to the pixel in the center between the two cross-correlated positions. In this manner, XC carpets can be generated for every possible pixel distance, with the AC carpet being the special case of zero distance. Pixel combinations that include diffusion barriers and lack molecule exchange appear as gaps with low correlation amplitudes. This has been demonstrated earlier via the analysis of spatial pair-correlation functions[13] obtained with scanning FCS setups that have been particularly useful for studying protein lateral diffusion in cell membranes[14–16]. In comparison to scanning-based techniques, the msFCCS approach benefits from complete spatio-temporal coverage. Along the measurement line, there are neither spatial nor temporal gaps for data acquisition and all combinations of lag time and displacement contribute to the calculated high-resolution XC curves.

To evaluate how a fluorescent particle 'senses' the obstacle density and the organization of the local environment (Fig. 1d), the mean squared displacement (MSD) and the corresponding time dependence of the diffusion coefficient were calculated from sets of AC and XC carpets optained by msFCCS. By applying Supplementary Equation (31) for a given pixel pair, an effective diffusion distance is calculated. It corresponds to the mean distance travelled by a molecule when detected in the first and subsequently in the second pixel, and an effective diffusion time calculated according to Supplementary Equation (32) that is approximately represented by the maximum of the XC function (Fig. 1b). The effective diffusion distances and times can readily be transformed into the MSD and the time-dependent diffusion coefficient $D(t)$ profile. In aqueous solution without obstacles, normal diffusion is observed, for which the diffusion coefficient is time-independent and the MSD scales linearly with time (Fig. 1d). In the presence of a significant concentration of obstacles, the mobility is reduced in a scale-dependent manner that is referred to as anomalous diffusion[17,18]. This mobility reduction is caused by collisions and binding reactions of particles with their cellular environment, which depend on the specific nature of the tracer molecule. Besides hydrodynamic effects, interactions between particles and obstacles can involve 'simple' hard sphere repulsion modulated by electrostatic and van-der-Waals' interactions as well as more long-lived binding reactions. Thus, $D(t)$ represents an apparent diffusion coefficient that includes information on the obstacle network encountered by a diffusing protein. To dissect the structural features of its environment, it is informative to visualize the scale-dependent diffusion coefficient $D(t)$ in a double-logarithmic plot versus translocation time t (Fig. 1d). For inert tracer molecules and an accessible space with fractal geometry[19,20], the diffusion coefficient follows a straight line in double-logarithmic representation. For random porous geometries, it is a sigmoidal-shaped function[7,21]. For very high obstacle densities, the molecules get trapped leading to corralled movements within a confined region[22].

Since our setup uses continuous line illumination, neighbouring pixels have overlap in the fluorescence signal they record. This results in an AC-type pseudo-correlation contribution for XC curves at short distances. To account for this contribution, a detailed characterization of the microscope's point-spread function (PSF) was carried out (Fig. 2a; Supplementary Notes 1 and 2; Supplementary Figs 1–3; Supplementary Tables 1 and 2). Instead of the commonly used three-dimensional Gaussian function, we implemented a double-cone shaped model function[23] for the PSF that provides a more accurate description (Supplementary Note 1). Slow-intensity fluctuations due to large-scale movements of cellular components and out-of-focus fluorescence bleaching were removed by Fourier filtering (Fig. 2b; Supplementary Note 3; Supplementary Figs 4–6). Instrumental setup and data analysis pipeline were validated with reference measurements of inert quantum dots (QDots) and TetraSpeck beads in buffer to ensure that the experimental XC curves were described accurately by the theoretical model functions for all detection volumes and correlation distances (Fig. 2c–e; Supplementary Note 4). The absolute diffusion coefficients obtained in these experiments were in excellent agreement with literature values (Table 1).

Permeability maps show local structural heterogeneity. The mobility of inert GFP monomers (GFP_1), trimers (GFP_3) and pentamers (GFP_5) was measured in the nucleus and cytoplasm of human U2OS cells. As a reference, the mobility of GFP_1 was also determined in aqueous solution. The msFCCS curves were acquired at about 50 positions that were equally distributed along a line of 10 μm in length. In aqueous solution, the diffusion coefficients of GFP_1 were independent of the translocation distance, with increasing s.d. due to decreasing signal-to-noise ratios at larger distances (Fig. 3a and Supplementary Table 3). In contrast, diffusion coefficients of GFP_1, GFP_3 and GFP_5 in the cytoplasm and nucleus decreased with increasing separation distance. This demonstrates that the diffusion process in cells was significantly slowed down in a length-scale-dependent manner and deviated from free diffusion. The mobility histograms for larger translocation distances were broadened and showed an increasing fraction of proteins with reduced mobility as compared with that measured on short time scales. Thus, the cellular interior appeared heterogeneous and some particles became at least transiently trapped. To quantitate the amount of trapped particles, we conducted complementary fluorescence recovery after photobleaching (FRAP) experiments (Fig. 3b and Supplementary Note 5). We first evaluated the post-bleach radial intensity profile[24] that yielded information about particles trapped for at least 100 ms (Supplementary Table 4). As a reference monomeric red fluorescent protein (RFP_1) was measured simultaneously with GFP_3 ($r_H \approx 5.5$ nm) and GFP_5 ($r_H \approx 7.9$ nm). RFP_1 has a similar hydrodynamic radius to GFP_1 ($r_H \approx 2.8$ nm) and can be spectrally separated from GFP_3 and GFP_5. Thus, it is a convenient internal standard to exclude experimental artifacts that might originate from focus drift, optical aberrations or cell motion. The amount of RFP_1 that was trapped for at least 100 ms in the nucleus was negligible (Fig. 3b). In contrast, significant fractions of about 6–8% trapped GFP_3 and

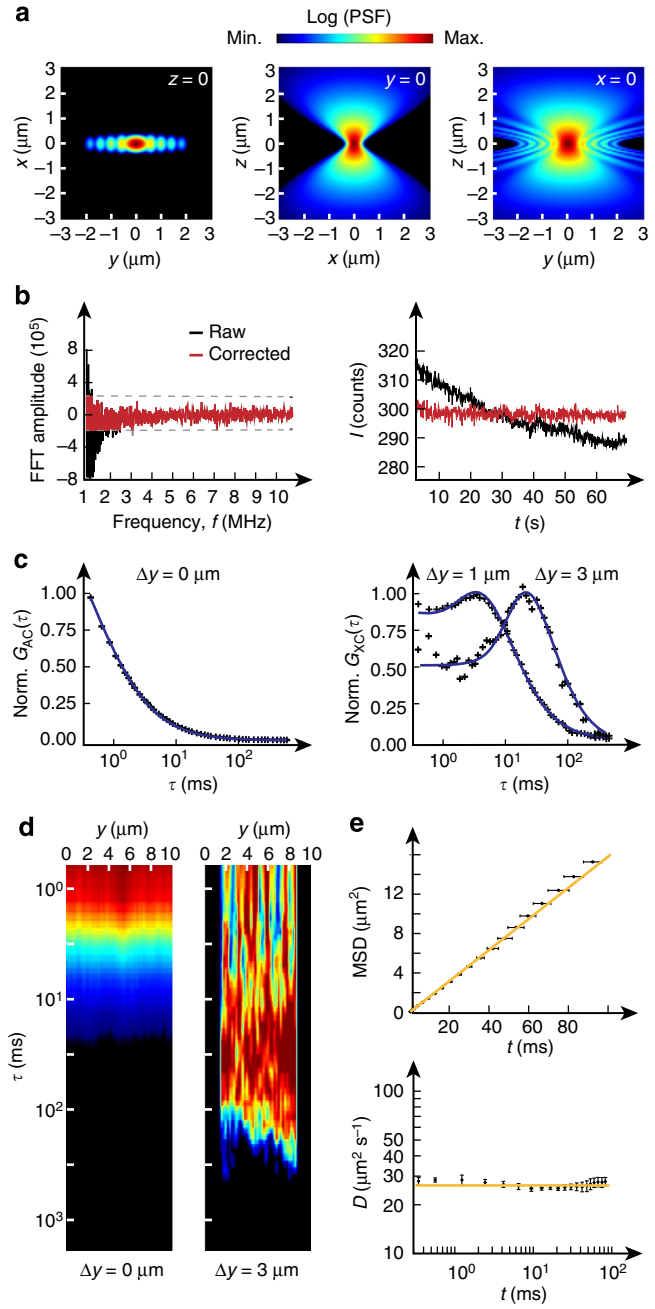

Figure 2 | Instrument characterization, signal processing and validation of the data analysis pipeline. (**a**) Approximation of the PSF of the line-confocal microscope as used for subsequent correlation analysis. (**b**) Fluorescence signal correction by Fourier filtering. Left: exemplary raw and corrected Fourier transformed fluorescence signal in the frequency domain. Right: fluorescence signal before and after signal correction in the time domain. (**c**) Experimental AC curve and XC curves for 1 and 3 µm diffusion distance for a reference measurement with 20 nM QDots in aqueous solution. Correlation curves were fitted with Supplementary Equation (22). (**d**) Experimental AC and XC carpet (3 µm) of QDots measured in water. (**e**) The MSD scales linearly with time for the QDot reference measurements in water as expected for free diffusion. Data are mean values ± s.e.m. ($n = 10$ measurements). Norm., normalized.

GFP_5 were present (Supplementary Table 4). To quantitate the amount of molecules trapped for at least 1 min, we conducted a conventional FRAP analysis of the average recovery curve that yielded hardly any trapped GFP_5 in the cytoplasm, while the immobile fraction of GFP_5 in the nucleus persisted. This suggests that the throat size χ of small pores that confine GFP_5 is similar to the hydrodynamic diameter of GFP_5, which equals 15.8 nm. In the nucleus, these throats seem to remain closed on the minute time scale, whereas corresponding regions in the cytoplasm open up faster so that trapping is detected only on the 100-ms time scale. The diffusion coefficients of RFP_1, GFP_3 and GFP_5 determined by FRAP using a bleach spot with a radius of 1.3 µm were in good agreement with the values obtained here by msFCCS (Table 1) and the values obtained recently by pixel-wise photobleaching profile evolution analysis[25] on the same length scale.

To map the spatial arrangement of regions with fast and slow protein transport, AC- and XC carpets were plotted for GFP_1 measurements in water, nucleus and cytoplasm (Fig. 3c). In the cytoplasm and particularly in the nucleus, protein mobility was reduced at a subset of positions. This mobility pattern indicated the presence of diffusion barriers created by inaccessible regions that hinder molecular transport as observed previously using scanning FCS followed by pair-correlation function analysis[13,16,26]. At the same time, the correlation carpets revealed large regions with high mobility in both cytosol and nucleus, representing extended accessible subcompartments that are separated by barriers. Furthermore, the heterogeneous amplitude values and diffusion times in the correlation carpets of GFP_1 in the nucleus indicate an increased heterogeneity of chromatin compared to the cytoplasmic environment, which is consistent with previous studies[27–29].

Scale-dependent mobility reveals a random obstacle structure. We determined the average scale-dependent mobility of GFP_1, GFP_3 and GFP_5 along a line positioned in the nucleus or cytoplasm to characterize the cellular environment from these proteins' points of view (Fig. 4a). Average AC and XC curves for exemplary distances are shown in Fig. 4b. In the XC curves, a peak was observed at the most frequent translocation time that shifts to larger diffusion times when increasing the separation distances as shown for 1.6 and 3.0 µm. The time dependence of the MSD or the diffusion coefficient retrieved from all XC curves obtained in at least 10 different cells from the human U2OS cell line were evaluated for each GFP multimer type and cellular compartment (Fig. 5a and Supplementary Note 6). The anomalous diffusion behaviour changed from GFP_1 to GFP_5, revealing a protein size dependence of the accessible cellular space. In general, the overall mobility in the nucleus and the cytoplasm were very similar, suggesting that chromatin and cytosolic obstacles have comparable effects on the translocations of proteins. The time dependence observed for the average diffusion coefficients displayed a sigmoidal shape in double-logarithmic representation. Thus, the cellular environment can be accurately described by a multi-scaling random obstacle organization rather than a single fractal or a corral structure with fixed size (Fig. 1d).

msFCCS retrieves parameters for a porous medium topology. The scale-dependent mobility of GFP monomer and multimers shown in Fig. 5a were accurately fitted by a simple model for diffusion in porous media consisting of randomly distributed obstacles[21]. It describes the apparent diffusion coefficient by the following equation:

$$D(t) = (D_0 - D_\infty)\exp\left(-\frac{4\sqrt{D_0 t}}{\sqrt{\pi}\lambda}\right) + D_\infty \qquad (1)$$

This relation contains the following fit parameters (Fig. 5b): (i) The microscopic diffusion coefficient D_0 of the particles observed at short time/length scales that describes their mobility in the

Table 1 | Mobility parameters obtained for different tracer molecules *in vitro* and in the nucleus of living cells.

	D ($\mu m^2 s^{-1}$)
msFCCS in vitro	
TetraSpeck beads (0.1 μm diameter)	4.4 ± 0.1*
QDot 525 streptavidin conjugate	31 ± 1*
msFCCS in living cells (nucleus)	
GFP_1	32 ± 3†
GFP_3	14 ± 2†
GFP_5	11 ± 1†
FRAP in living cells (nucleus)	
RFP_1	31 ± 7‡, §
GFP_3	15 ± 4‡, §
GFP_5	10 ± 1‡, ‖

FRAP, fluorescence recovery after photobleaching; GFP, green fluorescent protein; msFCCS, multi-scale fluorescence cross-correlation spectroscopy; RFP, red fluorescent protein.
Data were either obtained by msFCCS or FRAP with radial profile analysis. The results for TetraSpeck beads *in vitro* are in excellent agreement with the value $D = (4.4 \pm 0.7)\ \mu m^2 s^{-1}$ previously determined by dual-focus FCS and dynamic light scattering[69]. According to the measured diffusion coefficient of QDots, a hydrodynamic radius of $r_H = (7.8 \pm 0.3)$ nm was calculated that matches the specification value of (8.8 ± 1.3) nm given by the manufacturer (Invitrogen). msFCCS results in living cells agreed very well with FRAP experiments on the same length scale.
*Diffusion constants obtained by auto-correlation analysis are reported, since results were independent on time and length scale.
†Diffusion constants for msFCCS analysis with an effective distance of $d_{eff} = 1.2\ \mu m$.
‡FRAP results for a bleach circle radius of $w_b \approx 1.3\ \mu m$.
§An immobile fraction of (1 ± 1) % was found on the minute time scale.
‖An immobile fraction of (6 ± 1) % was found on the minute time scale.

absence of collisions with obstacles. (ii) The correlation length λ, which is a measure for the typical distance between obstacles. It is inversely proportional to the surface-to-volume ratio S/V. Since potential binding sites are located at the surface of intracellular structures, the parameter S/V is an important experimental readout for the characterization of target search processes as discussed below. The S/V ratio yields the structure's surface area that is sensed by diffusing proteins per unit volume (Supplementary Fig. 7). It depends on the volume fraction occupied by the obstacles and their spatial arrangement. For example, diffusing proteins sense less surface area in a clustered obstacle network than in a network of homogeneously distributed obstacles with the same obstacle volume fraction. (iii) The reduced macroscopic diffusion coefficient D_∞ measured at large time/length scales at which the MSD grows linearly with time. The ratio of D_0/D_∞ yields the retardation coefficient R. On the basis of R and the hydrodynamic radius of the tracer particles, the dimensions of fibre-shaped randomly placed obstacles can be derived according to the approach of Phillips[30] (Supplementary Note 7; Supplementary Fig. 8). From the microscopic diffusion coefficient D_0 compared with the diffusion coefficient in water, the apparent viscosity η_{app} of the bulk solution in the cell is obtained for each protein species.

The diffusion coefficient determined for GFP_1 in buffer equalled $D = 88 \pm 3\ \mu m^2 s^{-1}$ in good agreement with previously reported measurements[28]. The corresponding value in the cell was 1.3-fold lower (Table 2). This reduction reflects the subtle increase of the intrinsic viscosity of the cellular environment (Fig. 5c) due to the presence of small soluble factors. Thus, the intrinsic cellular viscosity is very similar to that of an aqueous solution. This agrees very well with previous results on the intracellular viscosity obtained from the rotational diffusion coefficient of GFP_1 (refs 31,32). For GFP_3 and GFP_5, the corresponding ratios increase to 1.8 and 2.7, indicating that the apparent viscosity for GFP_3 and GFP_5 is increased due to the presence of particles that appear as immobile obstacles to GFP_1.

The obstacle surface per volume S/V was higher for smaller molecules like GFP_1 (radius $r_H \approx 2.8$ nm) compared with larger molecules like GFP_5 ($r_H \approx 7.9$ nm). Thus, smaller molecules sample the surface of obstacles and barriers with higher resolution to 'see' more details and to access smaller pores and channels than larger molecules. Accordingly, molecules might visit different subsets of sites in dependence of their size, leading to partial unmixing of smaller and larger particles. The domain size that appears as a homogeneous environment to a particle diffusing with D_0 is related to the correlation length λ that scales with the inverse of the obstacle surface per volume S/V and equals 0.8 ± 0.2 μm for GFP_1 (Fig. 5c, Table 2). These regions are likely to represent lacunas with residual obstacles that appear mobile from the perspective of the GFP multimer. For translocation distances similar to λ the collision frequency with an apparently immobile obstacle increases considerably, while for distances above λ the average number of collisions per unit distance becomes constant and the time-dependent diffusion coefficient reaches the plateau value D_∞ (Fig. 5b). From the dependence of the retardation ratio $R = D_0/D_\infty$ on multimer size derived previously[30], we calculated that the obstacles occupy about $\Phi_0 \sim 15\%$ of the cellular space if a polymeric fibre-like structure is assumed (Fig. 5c; Supplementary Note 7). For this case, we determined a mean obstacle diameter d_{fiber} of about 12 ± 4 nm in the nucleus and 8 ± 4 nm in the cytosol.

Cytoskeleton and chromatin perturbations affect GFP mobility. To dissect the individual mobility contraints imposed by different cytoskeletal filaments, we conducted mobility measurements in cells treated with different drugs that disrupt the cytoskeleton (Fig. 6). We disassembled actin filaments with cytochalasin D (CYTD)[33], vimentin filaments with withaferin A (WFA)[34] and microtubules with nocodazole (NOC)[35]. Cytoskeletal filaments were efficiently disrupted as apparent on images acquired before and after drug treatment (Fig. 6 and Supplementary Fig. 9). Measurements of the time-dependent mobility of GFP_3 by msFCCS revealed moderate effects of cytoskeletal filament disassembly on GFP_3 transport (Fig. 6 and Table 2). On perturbation of actin microfilaments or vimentin filaments, lower retardation values were obtained that are indicative of a reduced obstacle concentration. Interestingly, no significant changes of GFP_3 mobility were observed on disruption of the microtubule network. This suggests that actin and intermediate filaments are the main fibre-shaped cytoskeletal structures that affect diffusion of GFP_3 in the cytoplasm. However, the moderate effects observed here suggest that other cytosolic components also influence molecular transport significantly.

To study the impact of chromatin on the mobility of inert particles, cells were treated with the drugs trichostatin A (TSA)[36,37] and chloroquine (CQ)[38]. Both substances lead to chromatin decondensation[36–41] by affecting internucleosomal interactions, either via histone hyperacetylation (TSA) or due to DNA intercalation and subsequent changes of DNA twist (CQ). On TSA and CQ treatment, the macrosocpic diffusion coefficient D_∞ of GFP_3 in the nucleus increased and the retardation R decreased (Fig. 7a,b and Table 2). The latter effect reflects a reduced obstacle density and was more pronounced for CQ treatment.

Collisions and binding interactions are dissected by msFCCS. To compare the mobility of inert GFP multimers to that of endogeneous proteins, we measured the time-dependent diffusion coefficient for fusion proteins in the nucleus and the cytoplasm. First, we studied the mobility of STAT2–GFP, which is mostly a

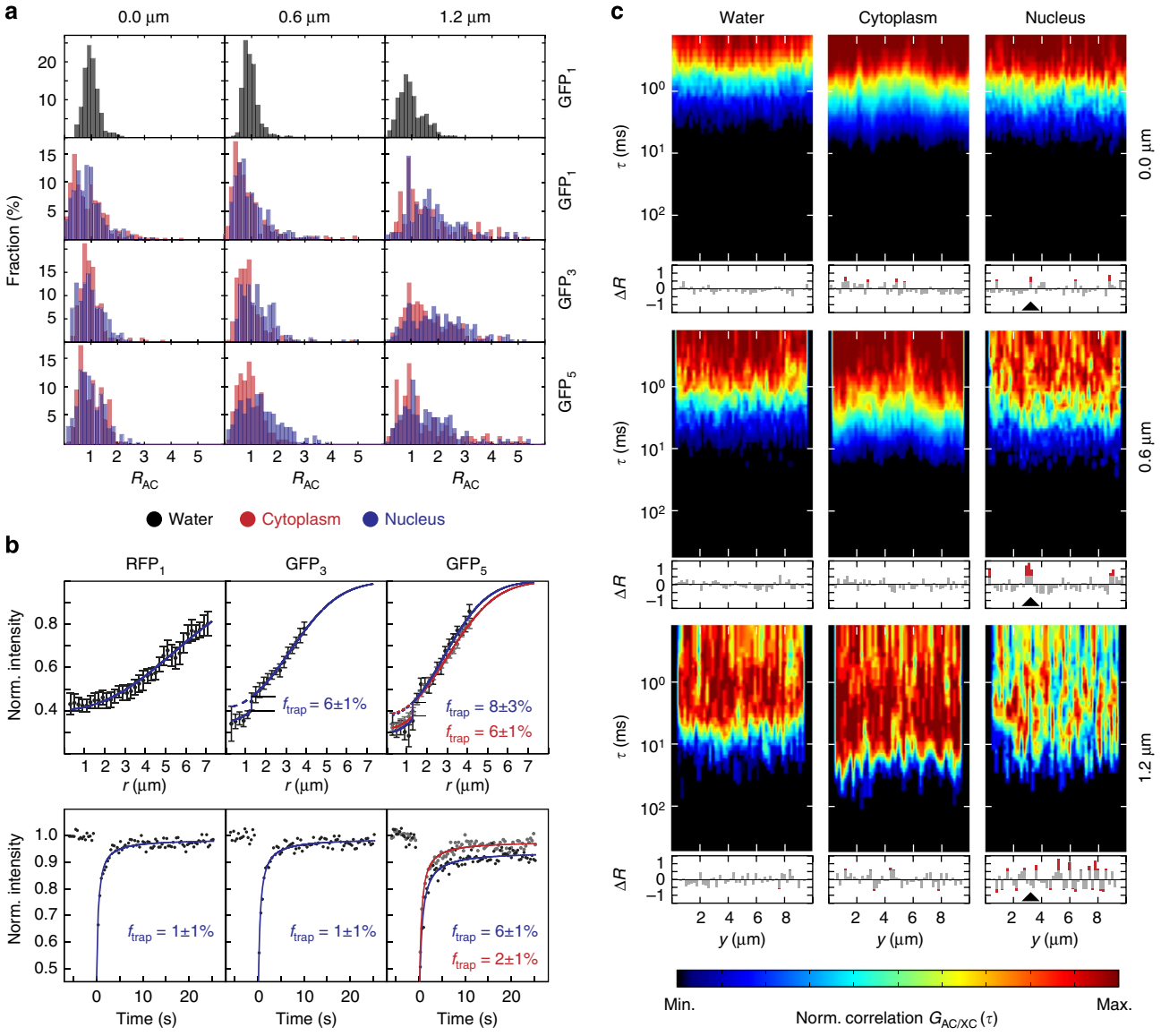

Figure 3 | Diffusion coefficients, trapped protein fractions and diffusion barrier density determined for GFP in living cells. (**a**) Histograms for the retardation coefficient $R_{AC} = D_{AC}/D$ ($n > 200$ values). The parameter R_{AC} corresponds to the translocation time of GFP monomer (GFP_1), trimer (GFP_3) and pentamer (GFP_5) molecules relative to the average value obtained from the AC analysis. Measurements were conducted at about 50 positions equally distributed on a 10 µm long line for separation distances of 0 µm (AC), 0.6 µm and 1.2 µm (XC) in water, the nucleus and the cytoplasm. (**b**) FRAP measurements of RFP_1 ($n = 12$ cells), GFP_3 ($n = 13$ cells) and GFP_5 ($n = 12$ cells). The fraction of trapped protein f_{trap} was obtained from the fit of either the post-bleach radial intensity profile after 100 ms with Supplementary Equation (29) (top row) or the average recovery curve with Supplementary Equation (30) (bottom row). Diffusion coefficients were determined from the average recovery curves. Data are mean values, error bars represent s.e.m. (**c**) Representative AC and XC carpets (0 µm, 0.6 µm and 1.2 µm separation distance) for GFP_1 in water, nucleus and cytoplasm. Regions with diffusion barriers can be identified from the fold increase of the translocation time ΔR plotted below the carpets. Negative ΔR values correspond to a decrease of the translocation time. An example for a diffusion barrier that is most pronounced for the 0.6 µm separation distance is marked with an arrowhead. Norm., normalized.

cytoplasmic protein that accumulates in the nucleus on stimulation to activate a subset of target genes[42,43]. Although STAT2–GFP has a molecular weight similar to GFP_5, its microscopic diffusion coefficient was significantly larger and very similar to that of GFP_3 (Fig. 7c and Table 2). This is in line with the expectation that STAT2–GFP has a more globular structure than the rod-like shaped GFP_5[27]. Apart from its inherently different shape, STAT2 sensed the cytoplasmic environment just like an inert tracer protein as apparent from its retardation and surface-to-volume ratio (Table 2). The comparison of STAT2–GFP, GFP_3 and GFP_5 demonstrates that the structural parameters obtained from the analysis of GFP multimers reflect the properties of the cellular interior as it is sensed by endogenous proteins. Thus, potential mobility differences arise from additional binding interactions with immobile obstacles in the cell.

To further dissect the contribution of obstacle collisions and binding events by msFCCS, we measured the mobility of a well-studied chromatin-interacting protein domain, the chromdomain of HP1β fused to GFP (CD–GFP). It has a molecular weight comparable to inert GFP_1 and binds to histone H3 molecules that carry a trimethylation modification at lysine 9 (ref. 44). For CD–GFP, the apparent time-dependent diffusion coefficient was determined in the nucleus and in the cytoplasm. As demonstrated above, both compartments impose similar constraints on the mobility of small molecules (Fig. 5), but the cytoplasm should be devoid of interaction partners of CD–GFP. As expected, the

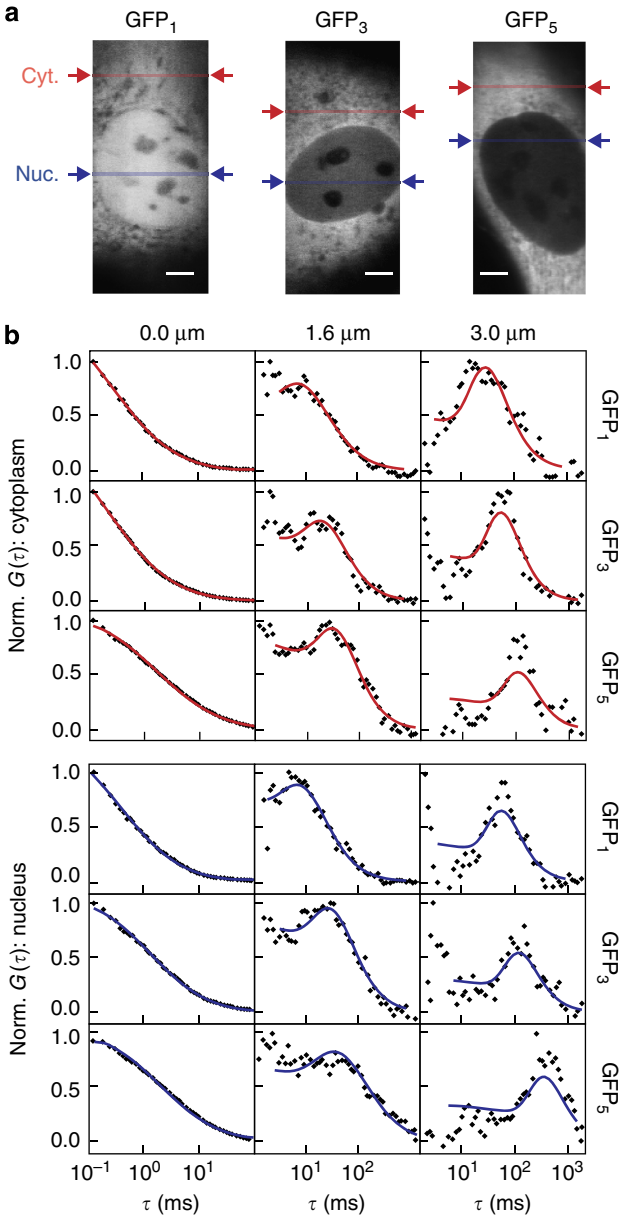

Figure 4 | Measurements on multiple length scales by msFCCS. (**a**) Line-confocal fluorescence images of representative U2OS cells expressing GFP_1, GFP_3 and GFP_5. The line positions for the measurement of AC and spatial XC functions in homogeneous regions of the nucleus and cytoplasm are indicated. (**b**) Representative average AC (0 µm) and XC (1.6 and 3 µm) curves obtained in cytoplasm (red) and nucleus (blue). For large diffusion distances, distinct peaks were visible in the diffusion time distributions that shift to larger translocation times for increasing diffusion distance. Solid lines represent the fitted model functions given by Supplementary Equation (22). Scale bar, 5 µm. Cyt, cytoplasm; Nuc, nucleus; Norm, normalized.

mobility of CD–GFP resembled that of GFP_1 in the cytoplasm (Fig. 7d). However, in the nucleus, the mobility of CD–GFP was largely different on both small and large scales due to chromatin binding. The structural parameters determined from the time-dependent diffusion coefficient on larger scales were similar to those for an inert GFP protein but with a significantly reduced macroscopic diffusion coefficient compared with similar-sized GFP_1 (Table 2). Thus, transient chromatin binding caused effective macroscopic diffusion behaviour with a reduced diffusion coefficient[45]. Interestingly, the reduced mobility of the bound CD-GFP pool strongly affected the $D(t)$ profile on small time scales. It resulted in a peak at 10 ms that was neither observed for inert proteins nor for CD–GFP in the cytoplasm (Fig. 7d). Thus, the msFCCS analysis conducted here allows for following the transition from the reaction-diffusion controlled regime on small scales to effective diffusion behaviour on large scales.

Discussion

Our approach to extract the scale-dependent mobility of proteins by msFCCS and to link it with intracellular architecture provides structural information on the nanometre scale that is given by the size of the GFP tracer molecules. It addresses a number of long-standing questions on how proteins sense the cellular interior that cannot be resolved by methods that operate on single length scales or in fixed cells:

(i) The local viscosity of the fluid embedding the cellular content was found to be only 1.3-fold larger than that of water for GFP_1, consistent with measurements of its rotational diffusion coefficient[31,32]. When evaluated over multiple scales, cytoplasm and nucleus imposed similar mobility constraints for particle sizes covered by GFP_1, GFP_3 and GFP_5 tracers with a slightly higher heterogeneity being present in the nucleus (Figs 3 and 5, Table 2). These finding are fully consistent with the single-length/time scale measurements conducted previously[27–29].

(ii) Diffusion barriers in both nucleus and cytosol were observed (Fig. 3). Thus, our msFCCS method extends the available repertoire of methods that study changes of molecular transport in the cell due to local structural alterations[13,16,26]. We found that particles of the size of a GFP pentamer can become trapped as inferred from the distribution of diffusion times in XC carpets (Fig. 3a) and we confirmed this finding by FRAP experiments (Fig. 3b) on different time scales.

(iii) Differently sized and shaped particles with hydrodynamic radii ranging from $r_H \approx 2.8$ nm (GFP_1) to $r_H \approx 7.9$ nm (GFP_5) 'sense' distinct structural environments with different surface-to-volume ratios and correlation lengths. While larger particles diffuse more slowly and become apparently excluded from certain regions, smaller particles can explore their local environment more thoroughly. We anticipate that this size-dependent difference can have a large impact on the target search mechanism and associated cellular functions, a prediction to be tested in dedicated experiments that are beyond the scope of the present study. Interestingly, the accessible cellular space in the nucleus is not a simple fractal, an issue that has been the subject of several previous studies[20,46–48]. Rather, the intracellular environment resembles a multi-scale porous medium formed by randomly distributed obstacles. The scale-dependent mobility of inert particles is accurately represented by a simple three-parameter model[21] (Figs 5–7). It describes two normal diffusion modes characterized by the microscopic and macroscopic diffusion coefficients D_0 and D_∞, respectively, which are connected by a crossover region. Within the latter region between the two diffusion regimes, the time-dependent diffusion coefficient can be approximated by a power law, which allows for retrieving an apparent fractal dimension. However, this approximation is only suitable on a particular length and time scale, and this scale is different for GFP_1, GFP_3 and GFP_5. Thus, we find no evidence for an invariant fractal dimension inherent in the architecture of the accessible space of the cell that could consistently explain the transport properties of differently sized particles. This agrees very well with recent simulation results of transport processes in porous media and polymer networks[49,50].

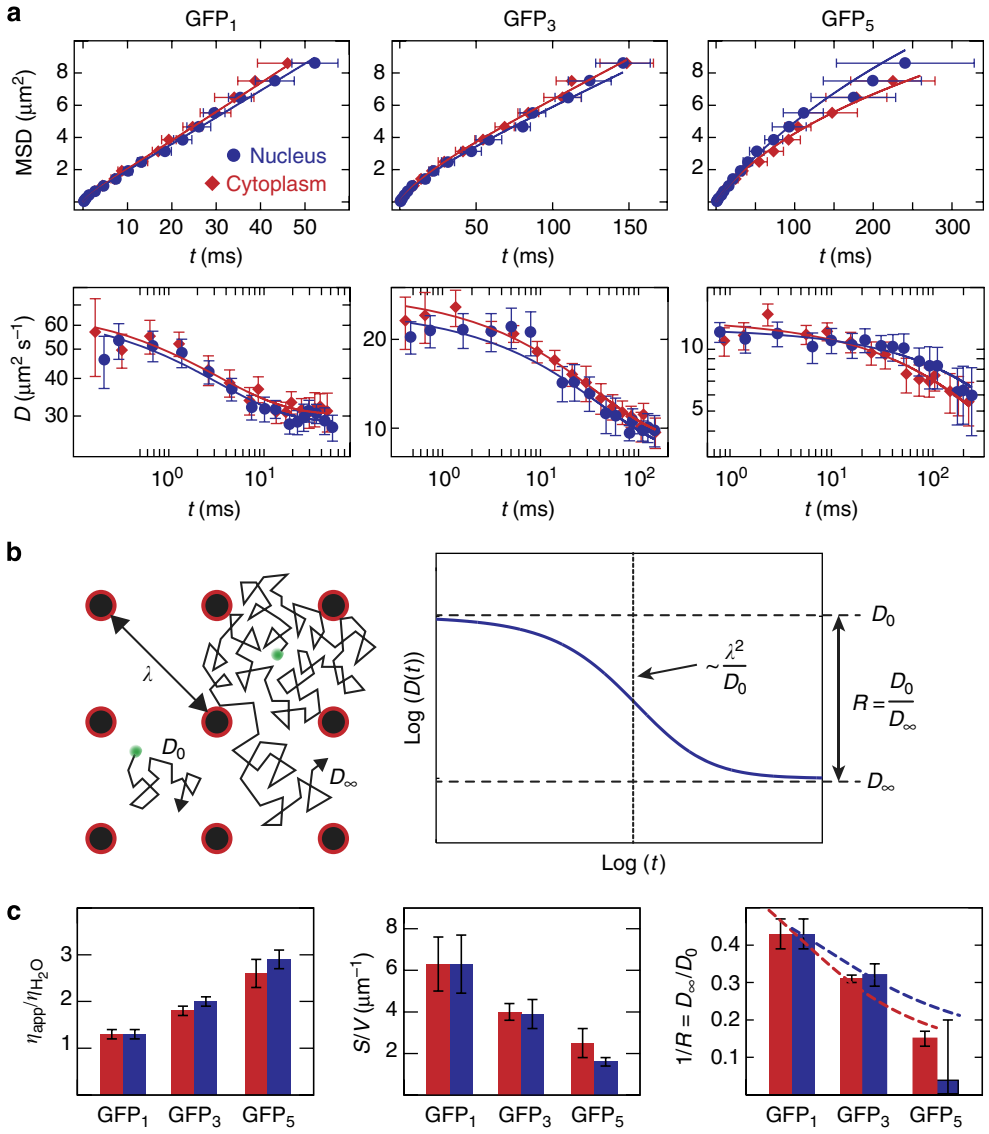

Figure 5 | Parameters for intracellular topology from time dependence of diffusion coefficients. (**a**) Average scale-dependent mobility of GFP_1 (Nuc: $n=14$ cells, Cyt: $n=13$ cells), GFP_3 (Nuc: $n=16$ cells, Cyt: $n=15$ cells) and GFP_5 (Nuc: $n=18$ cells, Cyt: $n=18$ cells) in the nucleus and cytoplasm. The time and length scale-dependent protein mobility is represented as the MSD (top row) or as the time-dependent diffusion coefficient $D(t)$ in double-logarithmic representation (bottom row). Data are mean values ± s.e.m. The solid lines represent a fit according to the random obstacle model in Equation (1). (**b**) Time-dependent diffusion coefficients were well described by a model for diffusion in a random porous medium. On small scales, molecules diffuse freely with D_0 (left). At a characteristic distance λ, they collide with an immobile obstacle. On large scales, this collision–diffusion process can be described with a reduced diffusion coefficient D_∞. The parameters of the model function used for fitting the time-dependent diffusion coefficient in porous media[21] are illustrated in double-logarithmic representation (right). The initial slope of the curve is related to the surface-to-volume ratio S/V (ref. 6). Extrapolation to short time scales yields the microscopic diffusion coefficient D_0 that would be measured in free solution, and extrapolation to large time scales yields the macroscopic diffusion coefficient D_∞ for translocations on large length scales. The ratio between both diffusion coefficients is referred to as retardation R. Based on these fit parameters, the correlation length λ can be calculated, which represents the length scale above which the medium appears homogeneous if it is sampled by a tracer of a given size. (**c**) Parameters characterizing the cellular environment derived from the fits of the time-dependent mobility of GFP multimers are the cellular viscosity η_{app}/η_{H_2O} relative to water, the surface-to-volume ratio S/V that is a measure for the apparent obstacle concentration and the retardation $R=D_0/D_\infty$. The dependence of R on the molecule size can be computed for polymeric obstacles to yield estimates for the average fibre diameter d_{fiber} and the obstacle volume fraction Φ_0 (ref. 30). Data are mean values ± s.e.m. Dashed lines represent fitted model functions given by Supplementary Equation (34).

(iv) Cytoskeletal actin, tubulin and intermediate filaments have only a moderate impact on protein transport in the cytoplasm as inferred from the effect of their depolymerization (Fig. 6, Table 2). This suggests that other cytoplasmic components like membrane-enclosed organelles represent obstacles that significantly influence cytoplasmic protein mobility. In contrast, drug-induced chromatin decondensation reduced the retardation of GFP_3 mobility considerably (Fig. 7a,b, Table 2), pointing to the chromatin network as the dominant obstacle towards translocations in the nucleus. When describing chromatin as a polymeric fibre-like obstacle structure we calculated that it occupies about 15% of the cellular space with a mean obstacle diameter of about 12 ± 4 nm (Fig. 5c; Supplementary Note 7). These values correspond to the known dimensions of open

Table 2 | Summary of the results obtained for the porous medium model.

Drug	D_0 (μm² s⁻¹)	D_∞ (μm² s⁻¹)	$R = D_0/D_\infty$	λ (μm)	S/V (μm⁻¹)
Cytoplasm					
GFP_1	69 ± 6	30 ± 4	2.3 ± 0.2	0.8 ± 0.2	6.3 ± 1.3
GFP_3	29 ± 1	9 ± 1	3.2 ± 0.1	1.5 ± 0.2	4.0 ± 0.4
CYTD	30 ± 1	13 ± 2	2.4 ± 0.3	1.5 ± 0.4	3.5 ± 1.0
WFA	26 ± 2	9 ± 1	2.8 ± 0.3	1.2 ± 0.3	4.8 ± 1.2
NOC	31 ± 2	9 ± 2	3.3 ± 0.5	1.5 ± 0.3	4.2 ± 0.9
GFP_5	14 ± 1	2 ± 1	6.6 ± 0.7	3.1 ± 0.9	2.5 ± 0.7
CD	51 ± 2	11 ± 2	2.3 ± 0.2	1.3 ± 0.3	3.9 ± 0.9
STAT2	24 ± 1	6 ± 1	3.8 ± 0.8	2.0 ± 0.8	3.3 ± 1.3
Nucleus					
GFP_1	66 ± 6	29 ± 3	2.3 ± 0.2	0.8 ± 0.2	6.3 ± 1.4
GFP_3	25 ± 2	8 ± 1	3.1 ± 0.3	1.6 ± 0.3	3.9 ± 0.7
TSA	30 ± 2	11 ± 3	2.8 ± 0.7	2.0 ± 0.8	2.9 ± 1.2
CQ	28 ± 1	13 ± 2	2.1 ± 0.3	1.7 ± 0.7	2.8 ± 1.2
GFP_5	13 ± 1	>1*	<33*	<5.5	1.6 ± 0.2
CD	51†	5 ± 2	9.4†	1.5 ± 0.1	5.4†,‡

CD, chromodomain; CQ, chloroquine; CYTD, cytochalasin D; GFP, green fluorescent protein; NOC, nocodazole; STAT2, signal transducer and activator of transcription 2; WFA, withaferin A; TSA, trichostatin A.
The parameters D_0, D_∞ and λ were determined by least-squares fitting of the model function for diffusion in porous media[21] to the measured time-dependent apparent diffusion coefficients of GFP_1, GFP_3, GFP_5, the chromodomain (CD) of HP1β or STAT2 in human U2OS cells. CD and STAT2 were fluorescently labelled with GFP. The retardation R and the surface-to-volume ratio $S/V = 9/\lambda\,(1-1/R)$ were calculated from the fit results. The intracellular structure was perturbed by treatment of the cells with CYTD, WFA, NOC, TSA or CQ as indicated.
*Since a significant fraction of GFP_5 was trapped in the nucleus according to our FRAP analysis, these values apply only for the mobile GFP_5 subpopulation.
†The microscopic diffusion coefficient of CD in the nucleus was fixed for least-squares fitting to that in the cytoplasm since these values should be similar in the short time-scale limit.
‡This value corresponds to an effective surface-to-volume ratio including chromatin binding interactions.

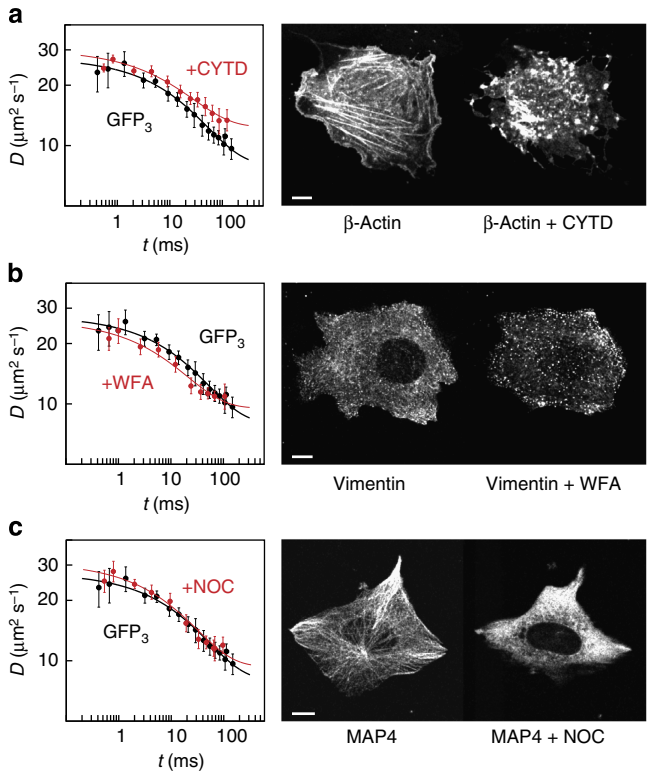

Figure 6 | Mobility of GFP_3 in the cytoplasm after disassembly of cytoskeletal filaments. Time-dependent diffusion coefficients measured in U2OS cells after perturbation of the cytoskeleton (red) compared with that in unperturbed cells (black, $n = 19$ cells). (**a**) Disruption of actin microfilaments by cytochalasin D ($n = 15$ cells). (**b**) Disruption of vimentin filaments by withaferin A ($n = 16$ cells). (**c**) Disruption of microtubules by nocodazole ($n = 14$ cells). Data are mean values ± s.e.m., fit curves correspond to Equation (1). Perturbations were validated based on the distribution of fluorescently tagged β-actin, vimentin or microtubule-associated protein 4 (MAP4), respectively. Scale bar, 10 μm.

nucleosome chains. For these, a diameter of 11 nm and an occupied volume fraction of ~18% in the nucleus was reported[51–53]. Furthermore, we conclude from our experiments that dynamic changes of the chromatin conformation can globally or locally regulate transport and target search processes in the nucleus. The msFCCS experiments conducted here in living cells are in excellent agreement with our previous conclusions on TSA-induced changes of chromatin conformation and accessibility[36,37].

(v) Endogenous proteins that do not interact with immobile obstacles, such as STAT2 in the cytoplasm, displayed time-dependent diffusion coefficients very similar to those of inert GFP multimers (Fig. 7c,d, Table 2). Thus, the cellular interior resembles a porous medium that imposes mobility constraints on all proteins in a size- and shape-dependent manner. We measured $S/V = 3.3 \pm 1.3\,\mu m^{-1}$ for STAT2–GFP versus $S/V = 6.3 \pm 1.3\,\mu m^{-1}$ for monomeric GFP in the cytoplasm. Thus, the accessible obstacle surface area scanned by the smaller GFP molecule was much larger than that of STAT2–GFP. In the presence of binding interactions with the obstacle scaffold, the time dependence of the apparent diffusion coefficient changed globally. This change is apparent from the comparison of the measurements of the chromatin-interacting HP1β chromodomain in the cytoplasm and the nucleus (Fig. 7d). Binding interactions of CD–GFP in the nucleus manifested themselves as a peak of the time-dependent diffusion coefficient, which was caused by slow fluctuations detected by msFCCS on short time scales. These signals might be linked to the confined motion of chromatin-bound CD–GFP molecules[45], temporal changes in the number of occupied binding sites or fluctuations caused by different photophysical properties of free and bound CD–GFP molecules[54]. We conclude that binding interactions alter the apparent diffusion coefficient in a scale-dependent manner, which can be exploited to study binding reactions by msFCCS.

The dynamic compartmentalization mechanism unravelled here is dependent on protein size as reflected in different S/V values for different proteins (Table 2). It might have important implications for the kinetics of enzymatic reactions, the target

search process of proteins and the formation of intracellular patterns. In particular, the preference of small enzymes to move inside distinct lacunas accelerates the binding of target sites in their local vicinity[1,55], which represents a simple but highly efficient mechanism to guide enzymatic reactions within a compartment that is not partitioned by membranes. In the nucleus, this mechanism might explain the differential enzymatic activity found in various parts of chromatin that serve distinct functions. One example for such a specialized chromatin domain is the perichromatin compartment[56] consisting of lacunas with reduced chromatin density and increased transcriptional activity. These loci are likely to appear as accessible regions with reduced obstacle concentration from the perspective of the GFP multimers (Fig. 8). In contrast, other chromatin subcompartments like lamina-associated domains[57] or pericentric heterochromatin[58] have an increased chromatin density and might act as obstacles. In the different nuclear domains, crucial enzymatic processes like transcription or recombination function very differently although they involve the same enzymes[59,60]. Thus, the size-dependent mobility and localization of proteins like polymerases or chromatin modifiers is an important aspect to establish spatial patterns. For example, the local enrichment or depletion of differently sized complexes with distinct enzymatic activity that range from 100 kDa to several MDa in molecular weight could generate specific patterns of chromatin modifications as discussed recently for histone demethylases[61]. Notably, cells can locally regulate the accessibility to different compartments by compaction and relaxation of their nanostructure as shown here in measurements of nuclear access in dependence of the histone acetylation state that we modulated by TSA treatment[37]. This type of transition from an open to a condensed chromatin structure has been observed during the differentiation of embryonic stem cells, which is accompanied by a reduction of global histone acetylation[62,63]. Interestingly, the open chromatin in embryonic stem cells was linked to an altered gene expression profile that is characterized by the low level expression of a large number of genes, referred to as 'promiscuous transcription', which likely correlates with an increased mobility and accessibility of protein factors. Furthermore, we found that treatment of cells with the DNA-intercalator CQ—a known drug against malaria[64]—decondensed chromatin and significantly enhanced protein transport within the nucleus. Such chromatin rearrangements naturally occur in response to DNA damage through the action of ATP-dependent chromatin remodellers and have been shown to be important for efficient DNA repair[39–41,65]. This suggests a functional link between chromatin architecture, protein transport and genomic stability. Likewise, other DNA intercalators like doxorubicin[66] that are used for anticancer

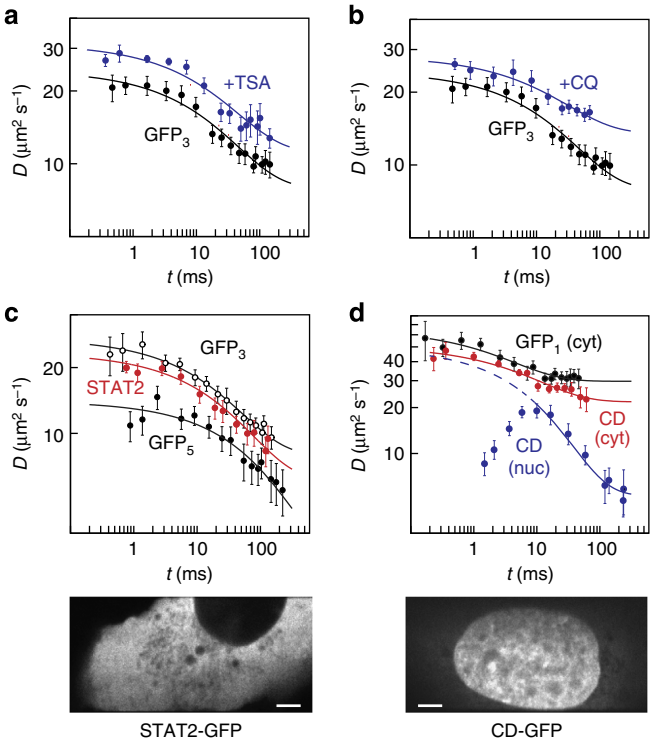

Figure 7 | Mobility of GFP_3 in the nucleus after decondensation of chromatin. (**a**) Time-dependent diffusion coefficient of inert GFP_3 in the nucleus of U2OS cells after perturbation of the chromatin structure with TSA (blue, $n=15$ cells) compared with that in unperturbed cells (black, $n=16$ cells). (**b**) Same as in **a** but after perturbation with CQ (blue, $n=13$ cells). (**c**) Mobility of STAT2 (red, $n=12$ cells), GFP_3 (white, $n=15$ cells) and GFP_5 (black, $n=18$ cells) in the cytoplasm of U2OS cells. The STFM image shows a representative cell expressing GFP-tagged STAT2. (**d**) Mobility of the chromodomain (CD) of HP1β in the cytoplasm (red, $n=11$ cells) and nucleus (blue, $n=11$ cells) compared with that of cytoplasmic GFP_1 (black, $n=13$ cells). The STFM image shows a representative cell expressing GFP-tagged CD. Data are mean values ± s.e.m., fit curves correspond to Equation (1). Scale bar, 5 µm.

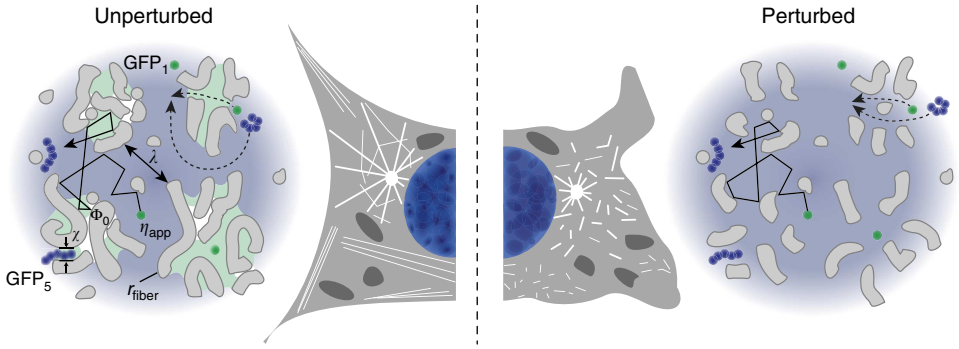

Figure 8 | The cellular interior appears as a porous medium formed by random obstacles. The correlation length λ for the distance between obstacles 'sensed' by a given protein is derived from the time dependence of its diffusion coefficient (Fig. 5).The parameter $\chi \sim 15$ nm is the estimated throat size of small pores that confine regions in the nucleus where GFP_5 (hydrodynamic radius $r_H \approx 7.9$ nm) is trapped while GFP_3 ($r_H \approx 5.5$ nm) remains mobile. Drug treatment induced structural changes as depicted on the right side of the scheme. Disassembly of cytoplasmic filaments resulted in a moderate increase of GFP_3 mobility (Fig. 6, Table 2). In contrast, chromatin decondensation increased GFP_3 mobility considerably (Fig. 7a,b, Table 2). Thus, chromatin is the major obstacle in the nucleus, whereas in the cytoplasm the cytoskeleton represents only one obstacle among others.

chemotherapies are expected to exert similar effects. The same applies to histone deacetylase inhibitors other than TSA that are used in cancer therapy[67]. Thus, the relation between drug-induced chromatin changes and altered protein transport unravelled here might be relevant to the clinical activities of several drugs in addition to their established mode of action. Accordingly, we anticipate that our approach to identify the internal cellular organization that governs the mobility and interactions of protein factors in living cells will provide new insight into the interplay between structure and function during development and its disease-related deregulation.

Methods

Fluorescence microscopy and spectroscopy. Imaging and msFCCS measurements were performed with a further developed microscope based on the previously described STFM setup[12]. The STFM continuously illuminates a line-shaped volume in the sample with laser light at 488 nm. To generate this illumination pattern, the Gaussian profile of a laser beam is cropped with a rectangular aperture, and cylindrical lenses are used to generate a laser beam profile that is focused in one direction and parallel in the perpendicular direction. By focusing this beam profile with a high-numerical objective lens into the sample, a line-shaped illumination volume is obtained. Emitted fluorescence signals from multiple detection volumes equally distributed along a line are recorded with a high quantum efficiency EM-CCD camera with 50-µs time resolution (iXon Ultra DU-897, Andor Technology). Fluorescence signals were recorded on a computer. An acousto-optical tunable filter (AOTFnC-400.650, AA Opto-Electronic) was integrated to minimize unintentional bleaching of fluorescence dyes by fine-adjustment of the illuminating laser beam power. For imaging, the illumination laser beam was deflected by a galvanometric mirror (GSI Lumonics) to scan the line in one direction and to acquire two-dimensional regions of interest.

Fluorescent samples, cell culture and msFCCS measurements. To determine the PSF of the STFM, yellow-green carboxylate-modified FluoSpheres (Molecular Probes) were fixated on poly-L-lysine (Sigma-Aldrich) coated cover slides and subsequently imaged. Alternatively, we used 13-nm-diameter fluorescent QDots with an emission maximum at 525 nm (yellow-green streptavidin conjugated QDots, Invitrogen) as fluctuating point light sources. QDots were immobilized on biotinylated bovine serum albumin coated LabTek chambered coverglasses (Nunc) by incubating a 0.3-nM QDot solution for 1 h. Unbound QDots were removed by rinsing the slides with 1 × PBS buffer and water.

The *in vitro* msFCCS measurements were conducted with a solution of QDots in water or purified GFP in 1 × PBS buffer at concentrations of 20 or 100 nM, respectively. For studies in living cells, plasmids encoding GFP_1, GFP_3, GFP_5[28], STAT2–GFP or CD–GFP were used. The STAT2–GFP plasmid was constructed by cloning the coding sequence of human STAT2 into a pEGFP-N1 vector backbone (Clontech) via Kpn I and Age I. For the CD–GFP plasmid, the chromodomain of human HP1β (aa 1-69) was cloned into the same vector via Bgl II and Hind III. For the expression of GFPs and GFP-tagged proteins, the respective plasmids were transfected into human U2OS cells (DSMZ, German Collection of Microorganisms and Cell Cultures) with effectene (Qiagen). Cells were cultured in Dulbecco's Modified Eagle's Medium supplemented with penicillin–streptomycin and 10% fetal bovine serum at 37 °C and 5% CO_2. In perturbation experiments, cells were incubated with either 8 µM cytochalasin D for 20 min, 10 µM nocodazole for 30 min, 2 µM withaferin A for 3 h, 400 nM TSA for 18 h or 80 µM CQ for 12 h. Perturbations of the cytoskeleton were validated based on the distribution of overexpressed β-actin-mRFP, mCherry-MAP4 or GFP-vimentin.

The FCS/msFCCS measurements were conducted in LabTek chambers with a data acquisition time of 1–3 min per measurement. For living cell experiments 10–20 cells were measured in two or three independent experiments. Only cells that did not change their position significantly during the measurement as judged by pictures taken before and after the experiments were used for the analysis. Measurements were conducted in homogeneous regions of nucleus and cytosol to avoid the influence of large vesicles, nucleoli or membranes that could cause intensity fluctuations.

Data processing and spatio-temporal analysis. FCS measurements in living cells frequently contain slow signal fluctuations due to external noise and movements of the cell or larger domains within it. In addition, bleaching of fluorescent dyes results in continuously decreasing fluorescence signals (Fig. 2b). These low frequency variations of the fluorescence signals were removed after Fast Fourier transformation (FFT) of the raw data (Supplementary Note 3; Supplementary Figs 4, 5 and 6). In Fourier space, the envelopes of FFT amplitude spectra were defined as mean values of equally large frequency intervals plus three times the corresponding s.d. These were fitted with an envelope model function for signals without intensity trends given by reference signals acquired for QDots in aqueous solution (Fig. 2b). High amplitudes at low FFT frequencies were truncated according to the envelope model function to remove the slow fluctuations, and the truncated FFT spectra were converted back to the time domain. Subsequently, the corrected fluorescence data were analysed by calculating the AC curves of each acquired signal and XC curves of each combination of signals from different detection volumes for a given diffusion distance as described previously[12]. The calculated AC and XC correlation curves were fitted by a model function (Supplementary Note 4). The model function required numerical solution of a double integral, which was accomplished with a multidimensional numerical integration algorithm extension to the GNU Scientific Library (GSL)[68]. Fitting of the non-linear model function to the calculated correlation curves was done with a least-squares minimization algorithm of the GSL. Correlation curves were fitted with self-written software in C ++ on a computer cluster. Results of the correlation analysis and least-squares fitting routine were further processed and plotted with MatLab (The MathWorks).

References

1. Benichou, O., Chevalier, C., Klafter, J., Meyer, B. & Voituriez, R. Geometry-controlled kinetics. *Nat. Chem.* **2,** 472–477 (2010).
2. Eltsov, M., Maclellan, K. M., Maeshima, K., Frangakis, A. S. & Dubochet, J. Analysis of cryo-electron microscopy images does not support the existence of 30-nm chromatin fibers in mitotic chromosomes *in situ*. *Proc. Natl Acad. Sci. USA* **105,** 19732–19737 (2008).
3. Wombacher, R. *et al.* Live-cell super-resolution imaging with trimethoprim conjugates. *Nat. Methods* **7,** 717–719 (2010).
4. Le Bihan, D. Looking into the functional architecture of the brain with diffusion MRI. *Nat. Rev. Neurosci.* **4,** 469–480 (2003).
5. Latour, L. L., Svoboda, K., Mitra, P. P. & Sotak, C. H. Time-dependent diffusion of water in a biological model system. *Proc. Natl Acad. Sci. USA* **91,** 1229–1233 (1994).
6. Mitra, P. P., Sen, P. N. & Schwartz, L. M. Short-time behavior of the diffusion coefficient as a geometrical probe of porous media. *Phys. Rev. B Condens. Matter* **47,** 8565–8574 (1993).
7. Sen, P. N. Time-dependent diffusion coefficient as a probe of geometry. *Concept. Magn. Reson. A* **23A,** 1–21 (2004).
8. Song, Y. Q., Ryu, S. & Sen, P. N. Determining multiple length scales in rocks. *Nature* **406,** 178–181 (2000).
9. Bacia, K., Kim, S. A. & Schwille, P. Fluorescence cross-correlation spectroscopy in living cells. *Nat. Methods* **3,** 83–89 (2006).
10. Capoulade, J., Wachsmuth, M., Hufnagel, L. & Knop, M. Quantitative fluorescence imaging of protein diffusion and interaction in living cells. *Nat. Biotechnol.* **29,** 835–839 (2011).
11. Machan, R. & Wohland, T. Recent applications of fluorescence correlation spectroscopy in live systems. *FEBS Lett.* doi: 10.1016/j.febslet.2014.03.056 (2014).
12. Heuvelman, G., Erdel, F., Wachsmuth, M. & Rippe, K. Analysis of protein mobilities and interactions in living cells by multifocal fluorescence fluctuation microscopy. *Eur. Biophys. J.* **38,** 813–828 (2009).
13. Digman, M. A. & Gratton, E. Imaging barriers to diffusion by pair correlation functions. *Biophys. J.* **97,** 665–673 (2009).
14. Ruan, Q., Cheng, M. A., Levi, M., Gratton, E. & Mantulin, W. W. Spatial-temporal studies of membrane dynamics: scanning fluorescence correlation spectroscopy (SFCS). *Biophys. J.* **87,** 1260–1267 (2004).
15. Ries, J., Chiantia, S. & Schwille, P. Accurate determination of membrane dynamics with line-scan FCS. *Biophys. J.* **96,** 1999–2008 (2009).
16. Di Rienzo, C., Gratton, E., Beltram, F. & Cardarelli, F. Fast spatiotemporal correlation spectroscopy to determine protein lateral diffusion laws in live cell membranes. *Proc. Natl Acad. Sci. USA* **110,** 12307–12312 (2013).
17. Wachsmuth, M., Waldeck, W. & Langowski, J. Anomalous diffusion of fluorescent probes inside living cell nuclei investigated by spatially-resolved fluorescence correlation spectroscopy. *J. Mol. Biol.* **298,** 677–689 (2000).
18. Weiss, M., Elsner, M., Kartberg, F. & Nilsson, T. Anomalous subdiffusion is a measure for cytoplasmic crowding in living cells. *Biophys. J.* **87,** 3518–3524 (2004).
19. Bunde, A. & Havlin, S. *Fractals and Disordered Systems* 2nd edn (Springer-Verlag, 1995).
20. McNally, J. G. & Mazza, D. Fractal geometry in the nucleus. *EMBO J.* **29,** 2–3 (2010).
21. Loskutov, V. V. & Sevriugin, V. A. A novel approach to interpretation of the time-dependent self-diffusion coefficient as a probe of porous media geometry. *J. Magn. Reson.* **230C,** 1–9 (2013).
22. Görisch, S. M. *et al.* Nuclear body movement is determined by chromatin accessibility and dynamics. *Proc. Natl Acad. Sci. USA* **101,** 13221–13226 (2004).
23. Dertinger, T. *et al.* Two-focus fluorescence correlation spectroscopy: a new tool for accurate and absolute diffusion measurements. *Chemphyschem.* **8,** 433–443 (2007).
24. Braga, J., Desterro, J. M. & Carmo-Fonseca, M. Intracellular macromolecular mobility measured by fluorescence recovery after photobleaching with confocal laser scanning microscopes. *Mol. Biol. Cell* **15,** 4749–4760 (2004).

25. Erdel, F. & Rippe, K. Quantifying transient binding of ISWI chromatin remodelers in living cells by pixel-wise photobleaching profile evolution analysis. *Proc. Natl Acad. Sci. USA* **109,** E3221–E3230 (2012).
26. Hinde, E., Cardarelli, F., Digman, M. A. & Gratton, E. *In vivo* pair correlation analysis of EGFP intranuclear diffusion reveals DNA-dependent molecular flow. *Proc. Natl Acad. Sci. USA* **107,** 16560–16565 (2010).
27. Dross, N. *et al.* Mapping eGFP oligomer mobility in living cell nuclei. *PLoS ONE* **4,** e5041 (2009).
28. Pack, C., Saito, K., Tamura, M. & Kinjo, M. Microenvironment and effect of energy depletion in the nucleus analyzed by mobility of multiple oligomeric EGFPs. *Biophys. J.* **91,** 3921–3936 (2006).
29. Moeendarbary, E. *et al.* The cytoplasm of living cells behaves as a poroelastic material. *Nat. Mater.* **12,** 253–261 (2013).
30. Phillips, R. J. A hydrodynamic model for hindered diffusion of proteins and micelles in hydrogels. *Biophys. J.* **79,** 3350–3353 (2000).
31. Luby-Phelps, K. *et al.* A novel fluorescence ratiometric method confirms the low solvent viscosity of the cytoplasm. *Biophys. J.* **65,** 236–242 (1993).
32. Swaminathan, R., Hoang, C. P. & Verkman, A. S. Photobleaching recovery and anisotropy decay of green fluorescent protein GFP-S65T in solution and cells: cytoplasmic viscosity probed by green fluorescent protein translational and rotational diffusion. *Biophys. J.* **72,** 1900–1907 (1997).
33. Schliwa, M. Action of cytochalasin D on cytoskeletal networks. *J. Cell Biol.* **92,** 79–91 (1982).
34. Grin, B. *et al.* Withaferin a alters intermediate filament organization, cell shape and behavior. *PLoS ONE* **7,** e39065 (2012).
35. Wadsworth, P. & McGrail, M. Interphase microtubule dynamics are cell type-specific. *J. Cell Sci.* **95,** 23–32 (1990).
36. Fejes Tóth, K. *et al.* Trichostatin A induced histone acetylation causes decondensation of interphase chromatin. *J. Cell Sci.* **117,** 4277–4287 (2004).
37. Görisch, S. M., Wachsmuth, M., Fejes Tóth, K., Lichter, P. & Rippe, K. Histone acetylation increases chromatin accessibility. *J. Cell Sci.* **118,** 5825–5834 (2005).
38. Krajewski, W. A. Alterations in the internucleosomal DNA helical twist in chromatin of human erythroleukemia cells *in vivo* influences the chromatin higher-order folding. *FEBS Lett.* **361,** 149–152 (1995).
39. Ogara, M. F. *et al.* Chromatin relaxation-mediated induction of p19INK4d increases the ability of cells to repair damaged DNA. *PLoS ONE* **8,** e61143 (2013).
40. Toiber, D. *et al.* SIRT6 recruits SNF2H to sites of DNA breaks, preventing genomic instability through chromatin remodeling. *Mol. Cell* **51,** 454–468 (2013).
41. Nakamura, K. *et al.* Regulation of homologous recombination by RNF20-dependent H2B ubiquitination. *Mol. Cell* **41,** 515–528 (2011).
42. Frahm, T., Hauser, H. & Köster, M. IFN-type-I-mediated signaling is regulated by modulation of STAT2 nuclear export. *J. Cell Sci.* **119,** 1092–1104 (2006).
43. Levy, D. E. & Darnell, Jr J. E. Stats: transcriptional control and biological impact. *Nat. Rev. Mol. Cell Biol.* **3,** 651–662 (2002).
44. Vermeulen, M. *et al.* Quantitative interaction proteomics and genome-wide profiling of epigenetic histone marks and their readers. *Cell* **142,** 967–980 (2010).
45. Erdel, F., Müller-Ott, K., Baum, M., Wachsmuth, M. & Rippe, K. Dissecting chromatin interactions in living cells from protein mobility maps. *Chromosome Res.* **19,** 99–115 (2011).
46. Bancaud, A. *et al.* Molecular crowding affects diffusion and binding of nuclear proteins in heterochromatin and reveals the fractal organization of chromatin. *EMBO J.* **28,** 3785–3798 (2009).
47. Bancaud, A., Lavelle, C., Huet, S. & Ellenberg, J. A fractal model for nuclear organization: current evidence and biological implications. *Nucleic Acids Res.* **40,** 8783–8792 (2012).
48. Lieberman-Aiden, E. *et al.* Comprehensive mapping of long-range interactions reveals folding principles of the human genome. *Science* **326,** 289–293 (2009).
49. Hofling, F. & Franosch, T. Anomalous transport in the crowded world of biological cells. *Rep. Prog. Phys.* **76,** 046602 (2013).
50. Fritsch, C. C. & Langowski, J. Anomalous diffusion in the interphase cell nucleus: the effect of spatial correlations of chromatin. *J. Chem. Phys.* **133,** 025101 (2010).
51. Maeshima, K., Hihara, S. & Eltsov, M. Chromatin structure: does the 30-nm fibre exist in vivo? *Curr. Opin. Cell Biol.* **22,** 291–297 (2010).
52. Fussner, E., Ching, R. W. & Bazett-Jones, D. P. Living without 30 nm chromatin fibers. *Trends Biochem. Sci.* **36,** 1–6 (2011).
53. Rippe, K. Dynamic organization of the cell nucleus. *Curr. Opin. Genet. Dev.* **17,** 373–380 (2007).
54. Yan, Y. & Marriott, G. Analysis of protein interactions using fluorescence technologies. *Curr. Opin. Chem. Biol.* **7,** 635–640 (2003).
55. Guigas, G. & Weiss, M. Sampling the cell with anomalous diffusion—the discovery of slowness. *Biophys. J.* **94,** 90–94 (2008).
56. Cremer, T. & Cremer, M. Chromosome territories. *Cold Spring Harb. Perspect. Biol.* **2,** a003889 (2010).
57. Kind, J. & van Steensel, B. Genome-nuclear lamina interactions and gene regulation. *Curr. Opin. Cell Biol.* **22,** 320–325 (2010).
58. Probst, A. V. & Almouzni, G. Pericentric heterochromatin: dynamic organization during early development in mammals. *Differentiation* **76,** 15–23 (2008).
59. Feuerbach, F. *et al.* Nuclear architecture and spatial positioning help establish transcriptional states of telomeres in yeast. *Nat. Cell Biol.* **4,** 214–221 (2002).
60. Agmon, N., Liefshitz, B., Zimmer, C., Fabre, E. & Kupiec, M. Effect of nuclear architecture on the efficiency of double-strand break repair. *Nat. Cell Biol.* **15,** 694–699 (2013).
61. Erdel, F., Müller-Ott, K. & Rippe, K. Establishing epigenetic domains via chromatin-bound histone modifiers. *Ann. NY Acad. Sci.* **1305,** 29–43 (2013).
62. Meshorer, E. *et al.* Hyperdynamic plasticity of chromatin proteins in pluripotent embryonic stem cells. *Dev. Cell* **10,** 105–116 (2006).
63. Gaspar-Maia, A., Alajem, A., Meshorer, E. & Ramalho-Santos, M. Open chromatin in pluripotency and reprogramming. *Nat. Rev. Mol. Cell Biol.* **12,** 36–47 (2011).
64. Slater, A. F. Chloroquine: mechanism of drug action and resistance in Plasmodium falciparum. *Pharmacol. Ther.* **57,** 203–235 (1993).
65. Erdel, F., Krug, J., Längst, G. & Rippe, K. Targeting chromatin remodelers: signals and search mechanisms. *Biochim. Biophys. Acta* **1809,** 497–508 (2011).
66. Pommier, Y., Leo, E., Zhang, H. & Marchand, C. DNA topoisomerases and their poisoning by anticancer and antibacterial drugs. *Chem. Biol.* **17,** 421–433 (2010).
67. Marks, P. A. Histone deacetylase inhibitors: a chemical genetics approach to understanding cellular functions. *Biochim. Biophys. Acta* **1799,** 717–725 (2010).
68. Galassi, M. *et al. Gnu Scientific Library: Reference Manual* (Network Theory Ltd, 2003).
69. Muller, C. B., Weiss, K., Richtering, W., Loman, A. & Enderlein, J. Calibrating differential interference contrast microscopy with dual-focus fluorescence correlation spectroscopy. *Opt. Express* **16,** 4322–4329 (2008).

Acknowledgements

We would like to thank Kendra Maaß and Harald Herrmann-Lerdon for help with cytoskeleton perturbations and are grateful to Masataka Kinjo, Hansjörg Hauser, Mario Köster, Peter Hemmerich, Ulrike Engel and Jana Hechler for plasmids. This work was funded within the projects EpiSys (0315502A/C) and ImmuoQuant (0316170B) of the German Federal Ministry of Education and Research (BMBF).

Author contributions

F.E. and K.R. conceived the project, coordinated the study and designed the experimental plan with help from M.B. and M.W. M.B. implemented the msFCCS system and conducted the experiments. M.B., F.E. and K.R. analysed the data and wrote the manuscript.

Additional information

Supplementary Information accompanies this paper at http://www.nature.com/naturecommunications

Competing financial interests: The authors declare no competing financial interests.

Reprints and permission information is available online at http://npg.nature.com/reprintsandpermissions/

How to cite this article: Baum, M. *et al.* Retrieving the intracellular topology from multi-scale protein mobility mapping in living cells. *Nat. Commun.* 5:4494 doi: 10.1038/ncomms5494 (2014).

Supplementary Information

Retrieving the intracellular topology from multi-scale protein mobility mapping in living cells

Michael Baum, Fabian Erdel, Malte Wachsmuth & Karsten Rippe

Supplementary Figures

1. Determination of PSF double-cone structural parameters from image stacks of fluorescent beads
2. Determination of the structural parameters of the PSF main and side lobes with high precision by spatial cross-correlation analysis
3. Calibration of PSF parameters according to *in vitro* reference measurements
4. Fluorescence signal correction in Fourier space
5. Validation of the Fourier transformation-based approach for signal correction
6. Comparison between moving average and Fourier transformation-based signal correction approaches
7. Sampling of intracellular surfaces in dependence of protein size
8. Interpolation of hindered diffusion parameters
9. Effect of different drugs on the cytoskeleton

Supplementary Tables

1. Experimentally determined structure parameters for the double-cone PSF
2. Summary of the determined PSF main and side lobe structural parameters
3. Statistical parameters of mobility histograms for GFP_1, GFP_3 and GFP_5
4. Results of FRAP measurements with radial profile intensity analysis

Supplementary Notes

1. Improved point spread function (PSF) model
2. Measurements of structural parameters for the improved PSF model
3. Signal correction in Fourier space
4. Correlation function for the improved PSF model
5. Fluorescence recovery after photobleaching analysis of GFP multimers
6. Effective translocation distance and time
7. Estimation of the occupied volume fraction and obstacle size

Supplementary References

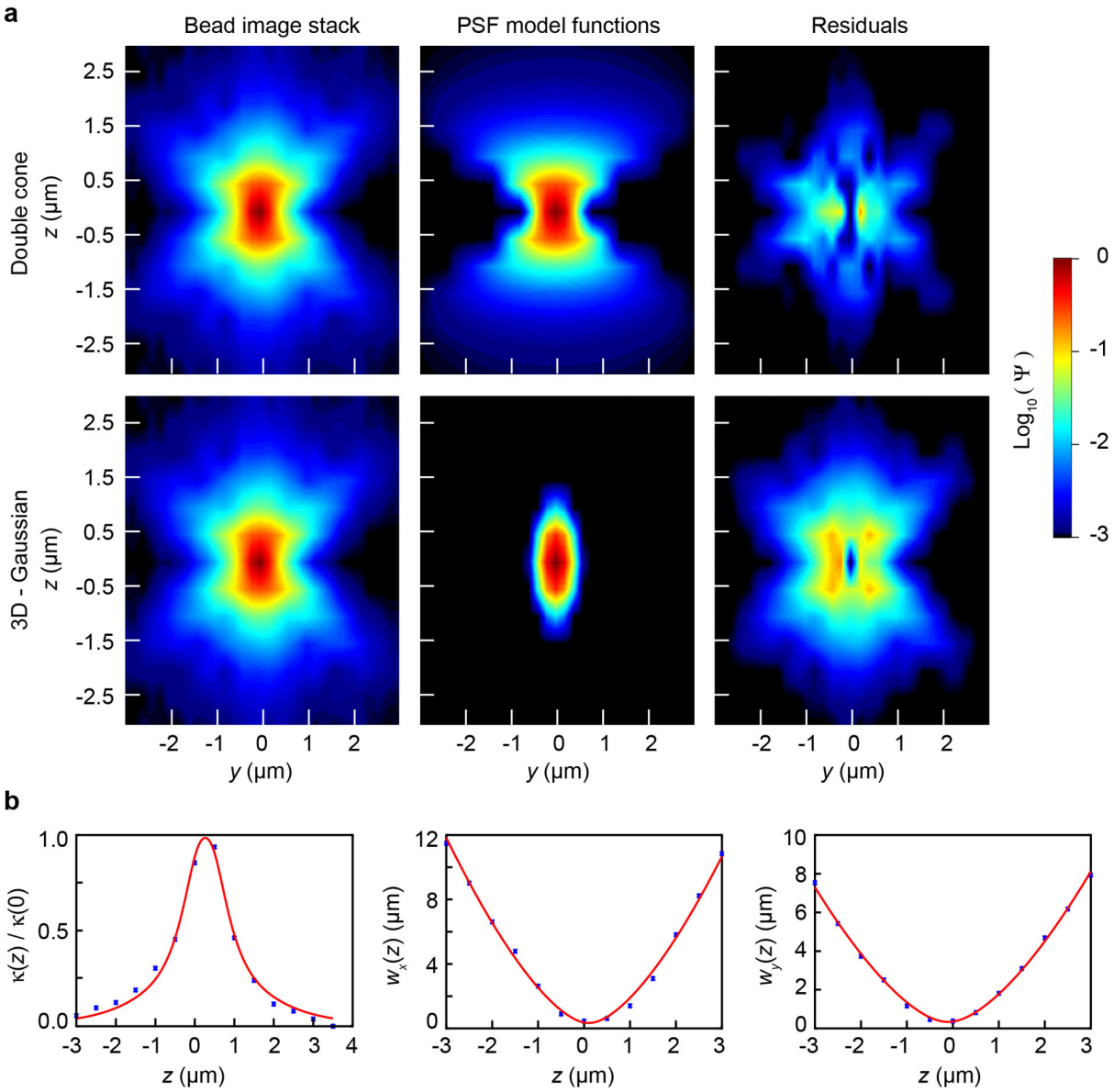

Supplementary Figure 1 | Determination of PSF double-cone structural parameters from image stacks of fluorescent beads. (**a**) Cross section through a representative image stack of a fluorescent bead for $x = 0$. As shown by the comparison of the fit and residuals the double-cone shaped model function (top row) showed a better description of the PSF than a three-dimensional Gaussian model (bottom row). (**b**) Least squares fitting of two-dimensional Gaussian functions to each slice of bead image stacks yielded the main lobe widths $w_x(z)$ and $w_y(z)$ in x- and y-direction as well as the mean intensity $\kappa(z)$ as functions of the axial position z. Double-cone structural parameters, i.e. cone angles represented by parameter k, cone curvature α and effective rectangular aperture lengths a and b, were determined by fitting theoretical model functions (red lines) to experimental data (blue dots). Fit results are listed in Supplementary Table 1.

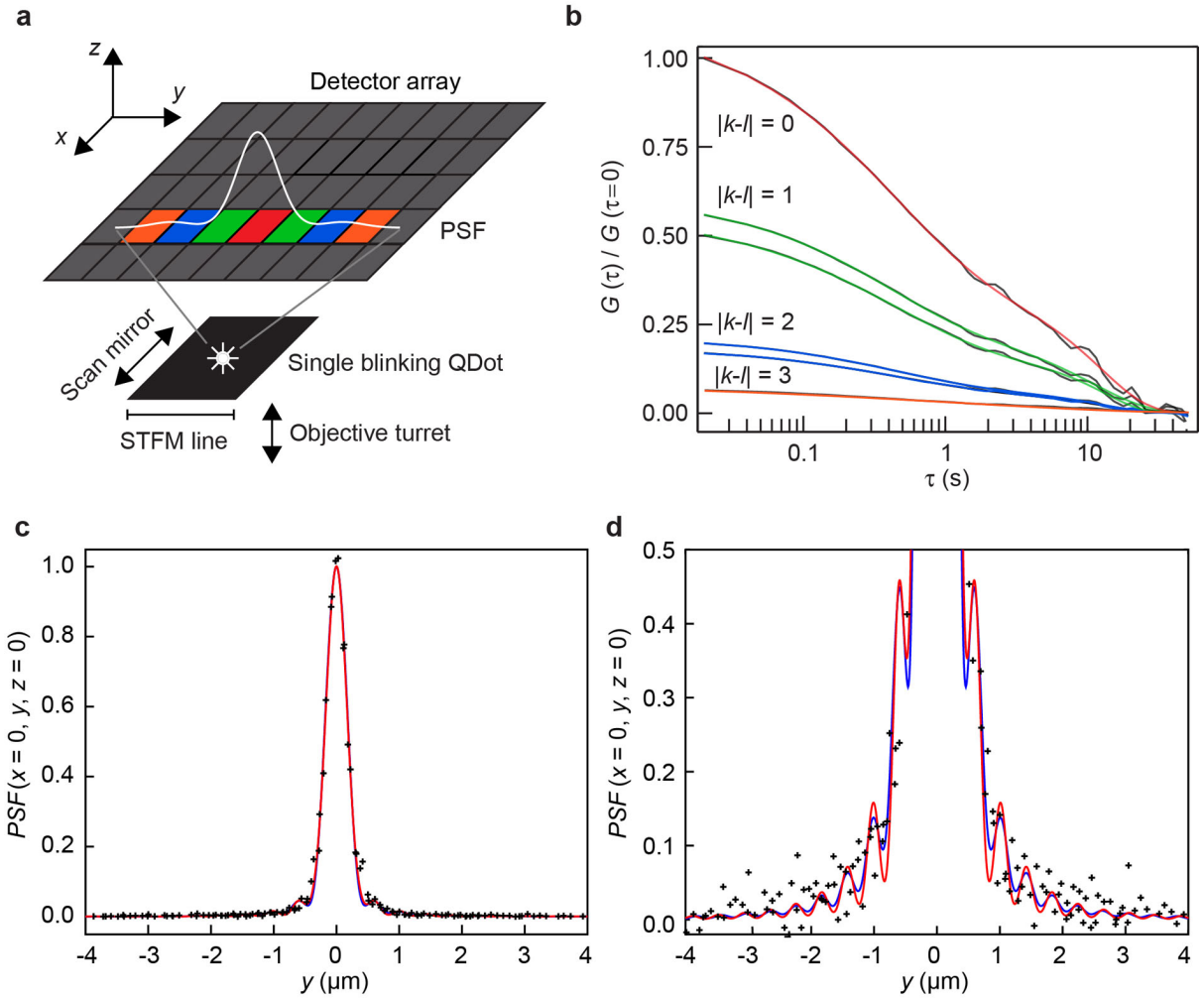

Supplementary Figure 2 | Determination of the structural parameters of the PSF main and side lobes with high precision by spatial cross-correlation analysis.

(**a**) Microscope setup for acquiring images and blink spectra of immobilized QDots. (**b**) Blink spectra of QDots for different cross-correlation distances $d = |k\text{-}l|$. (**c**) Measured PSF in line direction. PSF data (black crosses) from the spatial cross-correlation analysis were fitted to Supplementary Eq. 2 (red line). (**d**) Each lobe of the model function (red line) was approximated by a Gaussian function (blue line).

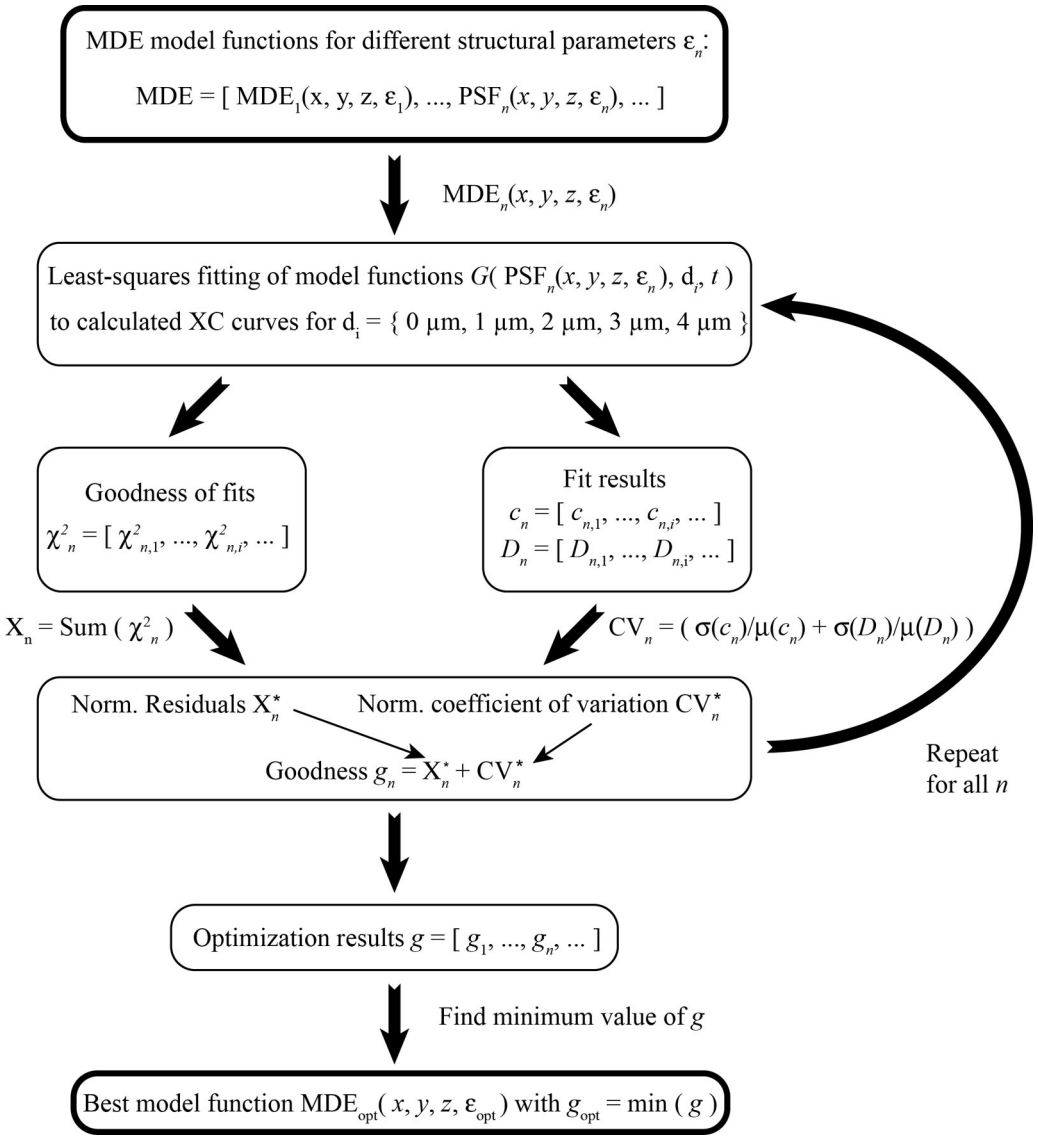

Supplementary Figure 3 | Calibration of PSF parameters according to *in vitro* reference measurements. We used correlation model functions G ($PSF(x, y, z, \varepsilon_n)$, d_i, τ) for different PSF geometries defined by structural parameters ε_n that matched the experimentally determined PSF structural parameters. The correlation model functions G ($PSF(x, y, z, \varepsilon_n)$, d_i, τ) were fitted to experimental correlation curves for different correlation distances d_i. In the next step, the goodness of the correlation function fits X_n and the coefficients of variation CV_n of the fit results were combined into a global fit quality parameter g_n. This procedure was repeated for each structural parameter combination ε_n. The PSF model function $PSF_{opt}(x, y, z, \varepsilon_{opt})$ yielding the best value of g_n was selected for least squares fitting of experimental msFCCS curves.

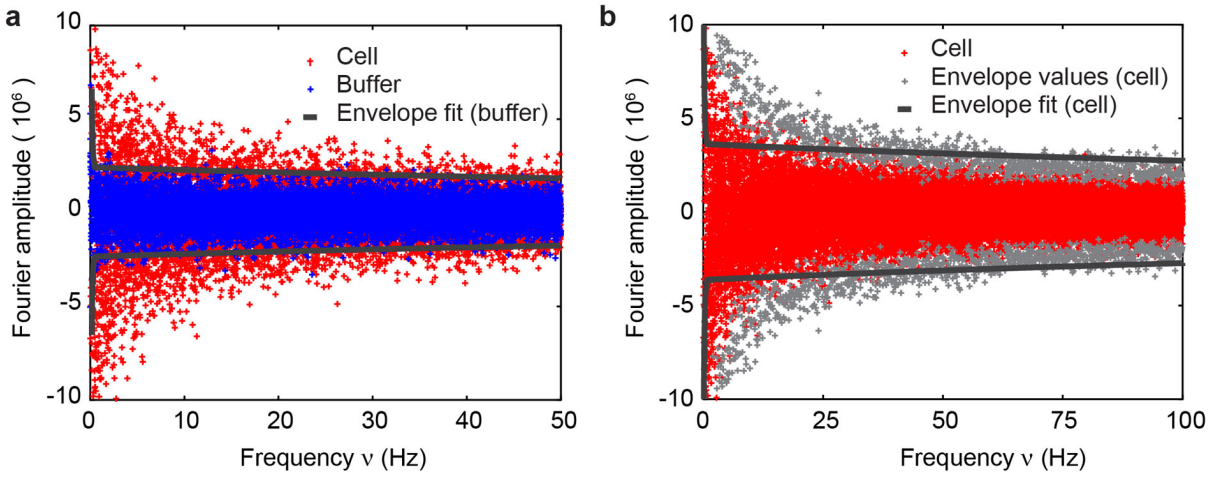

Supplementary Figure 4 | Fluorescence signal correction in Fourier space. (**a**) Fourier spectra of fluorescence signals obtained from GFP in aqueous glycerol solution (blue) and from GFP in the nucleus of a living cell (red). The Fourier spectrum obtained in cells showed higher amplitude values particularly at lower frequencies compared to a Fourier spectrum obtained from a measurement in buffer. The envelope of the spectrum in buffer, defined by Supplementary Eq. 18, was fitted by the envelope function (black) given by Supplementary Eq. 19. (**b**) The envelope function given in Supplementary Eq. 20 (black) was fitted to the envelope values e_i (grey) from the cell measurement (red) for subsequent cut-off correction.

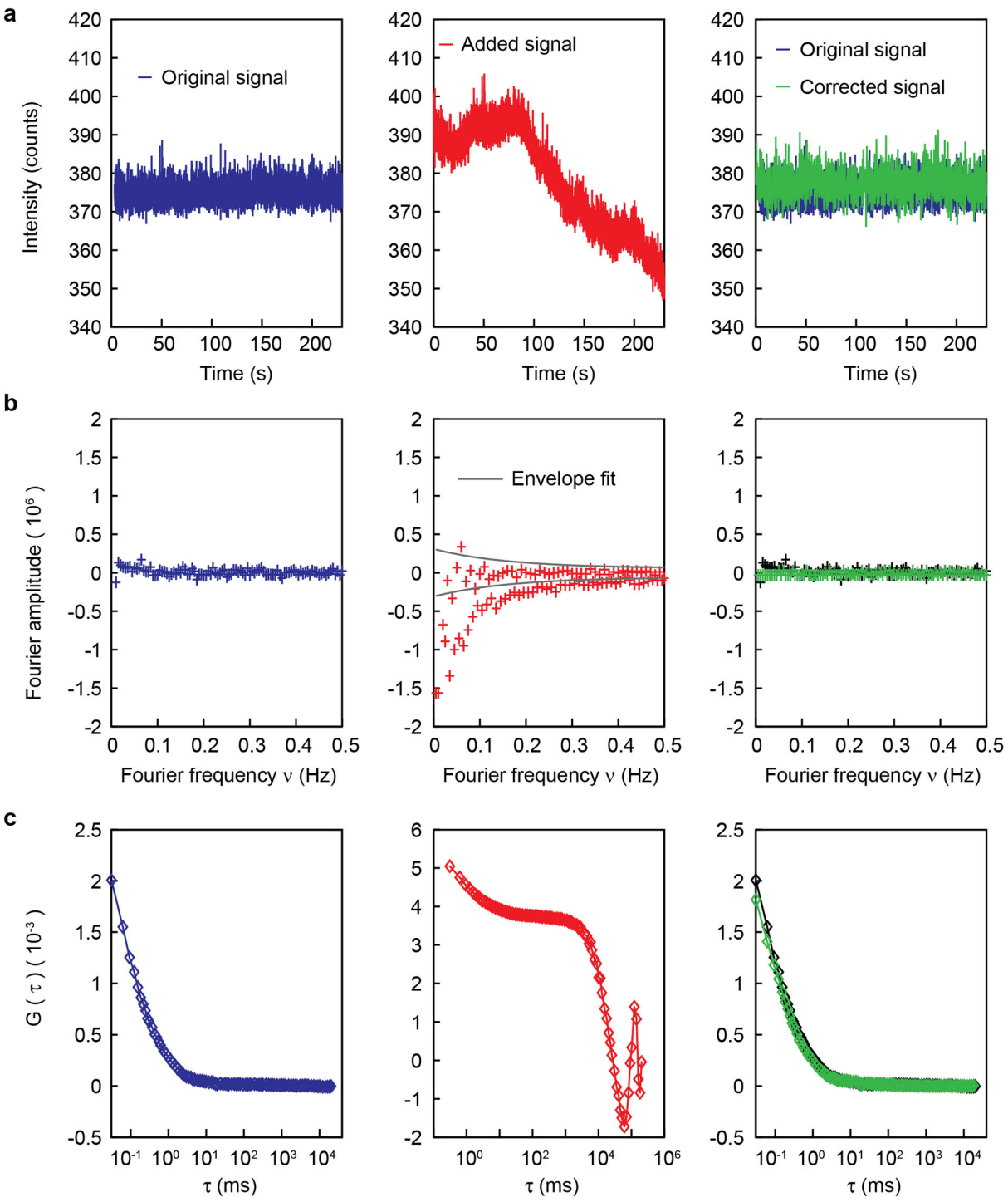

Supplementary Figure 5 | Validation of the Fourier transformation-based approach for signal correction. (**a**) An artificial trend signal function (center) was added to the experimentally measured fluorescence signal of diffusing QDots in aqueous solution (left). The original signal is very similar to the distorted signal that was corrected in Fourier space (right). (**b**) Fourier spectra for the original signal (left) and the distorted signal (center) are depicted. After cropping, the Fourier spectra are similar (right). (**c**) The auto-correlation curve of the fluorescence signal (center) is distorted, whereas after correction of the Fourier spectrum the original auto-correlation curve (left) is recovered (right).

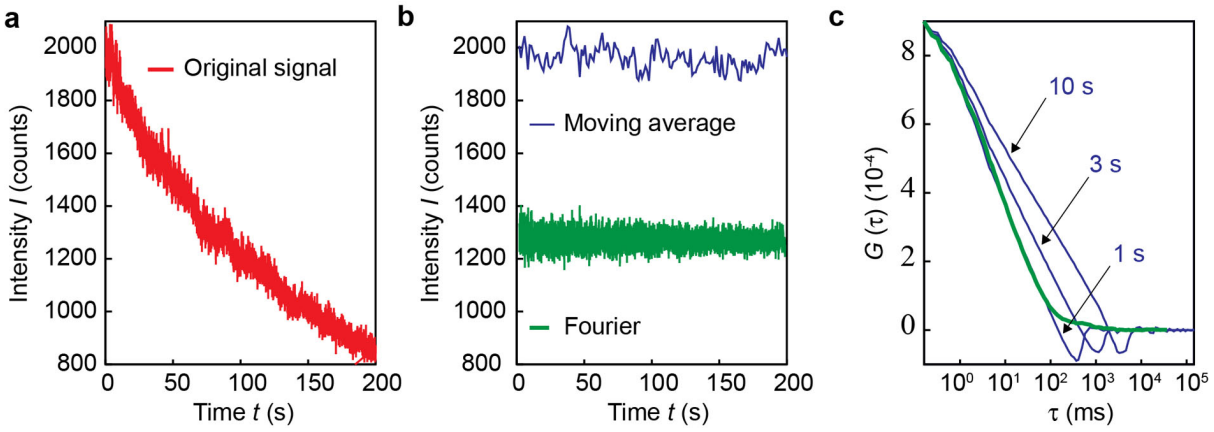

Supplementary Figure 6 | Comparison between moving average and Fourier transformation-based signal correction approaches. (**a**) Decaying fluorescence signal of a msFCCS measurement of the HP1-GFP fusion protein in the nucleus of a living cell. (**b**) Fluorescence signals corrected by the moving average approach with a correction window size of 1 s (blue) and by the Fourier transformation approach (green). (**c**) Calculated auto-correlation curves of moving average corrected fluorescence signals with 10 s, 3 s, and 1 s (blue) window size as well as a Fourier spectrum-corrected signal (green). The shape of the auto-correlation curves that were calculated based on signals corrected with the moving average strategy (blue) was dependent on window size. Furthermore, the curves (blue) show a dip at the time of half the window size, whereas no dip was present in the correlation curve of the Fourier corrected-signal. In moving average corrected signals, all correlations above time lags larger than half the window size were lost.

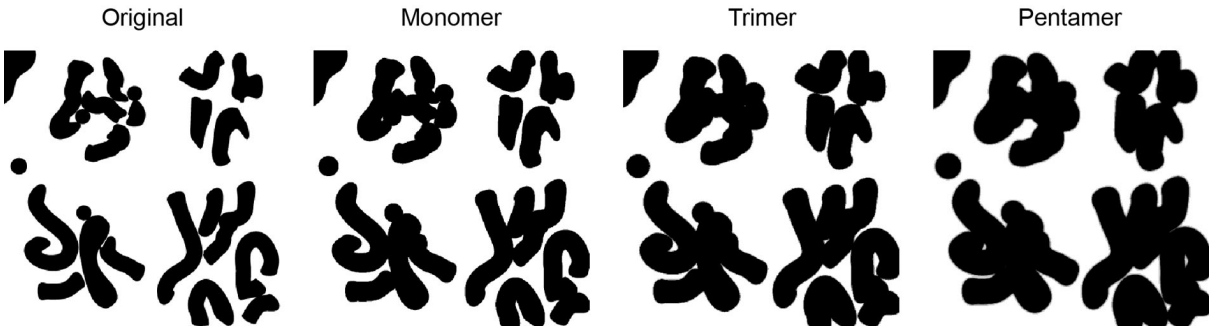

Supplementary Figure 7 | Sampling of intracellular surfaces in dependence of protein size. Small proteins can permeate into cavities and channels that are inaccessible for larger ones. Thus, small proteins sense the inner surface of dense intracellular structures, which results in increased surface-to-volume ratios *S*/*V*. The sensed surface is directly related to the number of visited potential binding sites. Images were generated by convolution of the structure shown left with a sphere of the radius of the respective GFP multimer. The fiber diameter of the original structure (left) corresponds to 25 nm.

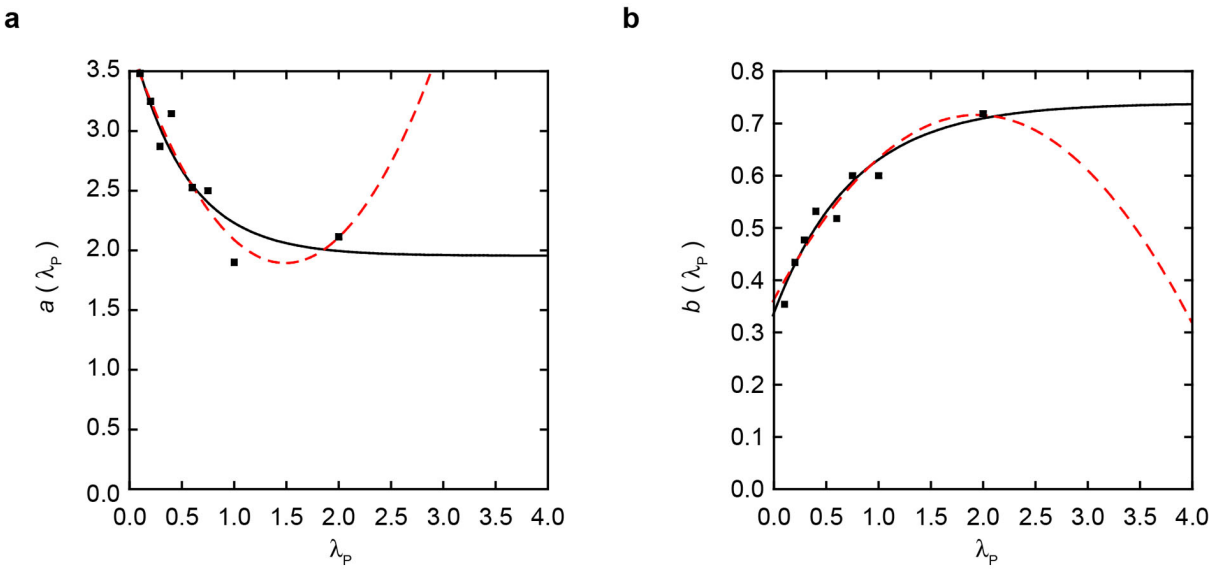

Supplementary Figure 8 | Interpolation of hindered diffusion parameters. The original polynomial interpolation for the hindered diffusion parameters *a* (**a**) and *b* (**b**) according to Phillips [1] (red dashed lines) were replaced by a modified exponential approximation (black lines). Both approximations yielded fits with good quality. The modified interpolation avoids diverging *a* values and negative *b* values for $\lambda > 2$, which would preclude extrapolation to larger λ values and might impair proper convergence of fitting routines.

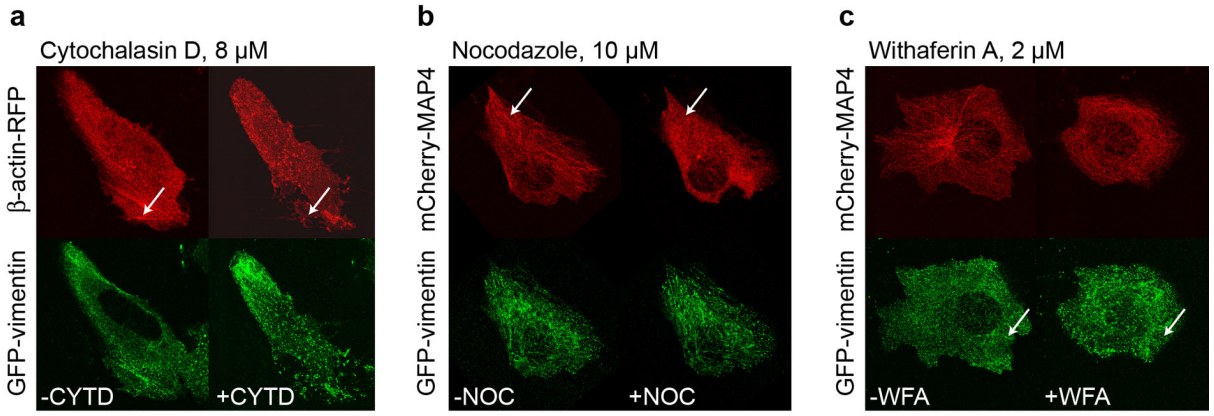

Supplementary Figure 9 | Effect of different drugs on the cytoskeleton. (**a**) Confocal images of a cell before (-CYTD) and after (+CYTD) treatment with 8 µM cytochalasin D. Actin filaments were stained with β-actin-mRFP and vimentin filaments were stained with GFP-vimentin. A white arrow indicates a region where disruption of the actin filaments was most pronounced. Vimentin filaments were also affected. (**b**) Images of a cell before (-WFA) and after (+WFA) treatment with 2 µM withaferin A. Microtubules were stained with mCherry-MAP4 and vimentin filaments were stained with GFP-vimentin. A white arrow shows a region where disruption of the vimentin filaments was observed. Microtubules were rearranged but not disrupted. (**c**) Images of a cell before (-NOC) and after (+NOC) treatment with 10 µM nocodazole. Microtubules were stained with mCherry-MAP4 and vimentin filaments were stained with GFP-vimentin. A white arrow highlights a region where disruption of the microtubules can be seen. Vimentin filaments were not disrupted.

Cone curvature	α_x	0.60 ± 0.03
	α_y	0.64 ± 0.02
Cone angle parameters (μm^{-1})	k_x	4.3 ± 0.4
	k_y	3.2 ± 0.1
Rectangular aperture size (μm)	a	5.7 ± 2.4
	b	0.6 ± 0.1

Supplementary Table 1 | Experimentally determined structural parameters for the double-cone PSF.

Lobe number	***n***	**0**	**1**	**2**	**3**	**4**
Amplitudes	A_n	1.000	0.044	0.016	0.007	0.002
Width	$w_{x,n}$ **(μm)**	0.19	1.25 $w_{x,0}(0)$			
	$w_{y,n}$ **(μm)**	0.32	0.53 $w_{y,0}(0)$			
Position	δ_n**(0) (μm)**	0	0.58	$\delta_1(0)$ + 0.41 (n-1)		

Supplementary Table 2 | Summary of the PSF main and side lobe structural parameters.

		0.0 µm			0.6 µm			1.2 µm		
		μ	σ	γ	μ	σ	γ	μ	σ	γ
GFP_1	**PBS**	1.0	0.3	1.0	1.0	0.3	1.7	1.0	0.6	0.8
	Cyt	1.0	0.7	1.5	1.0	0.8	2.5	1.7	1.1	1.2
	Nuc	1.0	0.6	1.1	1.1	0.7	1.4	1.9	1.0	1.1
GFP_3	**Cyt**	1.0	0.5	2.4	1.0	0.6	2.5	1.6	0.9	0.9
	Nuc	1.0	0.5	0.6	1.3	0.7	1.9	2.0	1.0	0.6
GFP_5	**Cyt**	1.0	0.4	0.5	1.0	0.5	0.8	1.6	1.2	1.3
	Nuc	1.0	0.5	0.7	1.4	0.8	0.7	1.7	1.0	1.3

Supplementary Table 3 | Statistical parameters of mobility histograms for GFP_1, GFP_3 and GFP_5. Measurements were conducted in aqueous solution (phosphate buffered saline, PBS), cytoplasm (Cyt), and nucleus (Nuc). Fitting of correlation functions for distances of 0.0 µm, 0.6 µm as well as 1.2 µm yielded histograms with mean value μ, standard deviation σ and skewness γ as indicated. Each histogram contained at least 200 values.

	Post-bleach radial profile			Average recovery curve	
	K_M	w_M (µm)	$f_{trap}^{100\ ms}$ (%)	D (µm^2 s^{-1})	$f_{trap}^{1\ min}$ (%)
RFP_1, Nuc	0.90	8.8	0	31 ± 7	1 ± 1
GFP_3, Nuc	0.88 ± 0.02	5.0 ± 0.1	6 ± 1	15 ± 4	1 ± 1
GFP_5, Nuc	0.98 ± 0.06	4.4 ± 0.2	8 ± 3	10 ± 1	6 ± 1
GFP_5, Cyt	0.83 ± 0.01	4.9 ± 0.1	6 ± 1	14 ± 4	2 ± 1

Supplementary Table 4 | Results of FRAP measurements with radial profile intensity analysis. Fit parameters based on the evaluation of the radial intensity profile 100 ms after the bleach (left) as well as the average recovery curve (right) are given. Measurements were carried out in the cytoplasm (Cyt) or the nucleus (Nuc) of U2OS cells. At least 10 measurements were conducted for each protein and cellular compartment.

Supplementary Note 1 | Improved point spread function (PSF) model

For a quantitative analysis of spatial cross-correlation curves, the point spread function (PSF) of the spatial and temporal fluctuation microscope (STFM) had to be described with an improved model function to correctly account for autocorrelation (AC)-type contributions due to spatially overlapping detection volumes. The PSF of confocal microscopes in general form is given as the product of illumination and detection PSF

$$PSF(\mathbf{r}) = PSF_{\mathrm{ill}}(\mathbf{r}) \cdot PSF_{\mathrm{det}}(\mathbf{r}). \tag{1}$$

For fluorescence correlation spectroscopy (FCS) with conventional (point illumination and detection) confocal microscopy setups with high numerical aperture (NA) objective lenses, the PSF can be approximated by rotationally symmetric two-dimensional Gaussian functions in the focal plane, since diffraction rings of the illumination PSF and the detection PSF interfere destructively. However, the diffraction pattern surrounding the central main lobe cannot be neglected if the illumination PSF is constant in one direction. The PSF of the microscope used here is theoretically described by a non-paraxial PSF model [2] in the focal plane that is given by Supplementary Eq. 2

$$\begin{aligned} PSF_{\mathrm{NP}}(x,y,z) = &\left| \int_{-\alpha}^{\alpha} \sqrt{\cos(\Theta)} \exp\left(-ik_{\mathrm{ex}} x \sin(\Theta)\right) \exp\left(-ik_{\mathrm{ex}} z \cos(\Theta)\right) k_{\mathrm{ex}} \cos(\Theta) d\Theta \right|^2 \\ \times &\int_{-s}^{s} \left| \int_{0}^{\alpha} \sqrt{\cos(\Theta)} J_0\left(k_{\mathrm{em}} \sin(\Theta) \sqrt{y^2 + (x - x_s)^2} \right) \exp\left(-ik_{\mathrm{em}} z \cos(\Theta)\right) k_{\mathrm{em}} \sin(\Theta) d\Theta \right|^2 dx_{\mathrm{s}} \end{aligned}. \tag{2}$$

Here, x and y are the axes perpendicular to and along the illumination line, respectively, and k_{ex} and k_{em} are the excitation and emission wave numbers, respectively. We approximated this PSF model in the focal plane by a central asymmetric two-dimensional Gaussian function surrounded by four low-amplitude asymmetric two-dimensional Gaussian functions on each side in direction of the illumination line. The central main lobe is elongated in y-direction along the line, whereas the side lobes are elongated in x-direction perpendicular to the line. In axial direction, the PSF is described by a double-cone shaped function [3]. The complete PSF can be approximated by

$$\Psi(\mathbf{r}) = \sum_{n=-4}^{4} \psi_n(\mathbf{r}), \tag{3}$$

where each lobe ψ_n is described

$$\psi_n(\mathbf{r}) = \frac{A_n\ \kappa(z)}{w_{x,n}(z) w_{y,n}(z)} \exp\left(-2\frac{x^2}{w_{x,n}^2(z)} - 2\frac{(y - y_n(z))^2}{w_{y,n}^2(z)} \right). \quad (4)$$

The functions $w_{x,n}(z)$ and $w_{y,n}(z)$ in Supplementary Eq. 4 describe the width of the n^{th} PSF lobe at axial position z:

$$w_{x,n}(z) = w_{x,n}(0) \cdot \left(1 + \left(k_x z\right)^2\right)^{\alpha_x}, \quad (5)$$

$$w_{y,n}(z) = w_{y,n}(0) \cdot \left(1 + \left(k_y z\right)^2\right)^{\alpha_y}. \quad (6)$$

Further, the parameter A_n gives the amplitude and $y_n(z)$ the center position of the two-dimensional Gaussian function describing the n^{th} PSF lobe in a cross section through the PSF at a distance z from the focal plane:

$$y_n(z) = y_n(0) \cdot \left(1 + \left(k_y z\right)^2\right)^{\alpha_y}. \quad (7)$$

The structural parameters k_x, k_y, α_x and α_y are determined by fitting the model functions to acquired three-dimensional image stacks of the PSF. Out-of-focus light is blocked by a slit of width a in confocal position and by detection on a quadratic pixel of the EM-CCD camera detection array with side length b. Thus, the microscope's resolution in axial direction is improved by reducing the PSF extension, and the contrast is enhanced. The reduction of the PSF in axial direction can be calculated as follows: Without a confocal slit, the PSF of the STFM is described by

$$\tilde{\Psi}(\mathbf{r}) = \sum_{n=-4}^{4} \tilde{\psi}_n(\mathbf{r}), \quad (8)$$

with the lobe function

$$\tilde{\psi}_n(\mathbf{r}) = \frac{\psi_n(\mathbf{r})}{\kappa(z)} = \frac{A_n}{w_{x,n}(z) w_{y,n}(z)} \exp\left(-2\frac{x^2}{w_{x,n}^2(z)} - 2\frac{(y - y_n(z))^2}{w_{y,n}^2(z)} \right). \quad (9)$$

The fraction of fluorescence light from an axial position *z* that can pass through the confocal slit aperture is given by

$$\kappa(z) = \frac{\int_{-a/2}^{a/2}\int_{-b/2}^{b/2}\tilde{\Psi}(\vec{r})dxdy}{\int_{-\infty}^{\infty}\int_{-\infty}^{\infty}\tilde{\Psi}(\vec{r})dxdy}. \tag{10}$$

The PSF side lobes in Supplementary Eq. 10 can be neglected, because in this approximation the PSF is cropped by the confocal slit and only the main lobe contribution remains. Thus, the maximum of the PSF at a distance *z* from the focal plane is given by

$$\kappa(z) = \frac{\int_{-a/2}^{a/2}\int_{-b/2}^{b/2}\tilde{\psi}_0(\vec{r})dxdy}{\int_{-\infty}^{\infty}\int_{-\infty}^{\infty}\tilde{\psi}_0(\vec{r})dxdy} = erf\left(\frac{a}{\sqrt{2}w_{x,0}(z)}\right)erf\left(\frac{b}{\sqrt{2}w_{y,0}(z)}\right). \tag{11}$$

Supplementary Note 2 | Measurements of structural parameters for the improved PSF model

Determination of the axial PSF geometry from imaging fluorescent beads

Image stacks of immobilized 100 nm fluorescent beads were acquired to determine the geometry of the STFM's PSF in axial direction. Each slice of the image stack was approximated with an asymmetric two-dimensional Gaussian model function by least squares fitting with the Matlab software (MathWorks). We determined the width $w_x(z)$ in x- and $w_y(z)$ in y-direction as well as the mean intensity $\kappa(z)$ as a function of the axial position z (Supplementary Fig. 1). Supplementary Eq. 5, 6 and 7 were fitted to the measured profiles. The resulting structural parameters a, b, α_x, α_y, k_x and k_y are summarized in Supplementary Table 1. For comparison, a one-dimensional Gaussian function was fitted in each spatial dimension of the acquired image stacks. Resulting fit parameters were the e^{-2} - radii $w_{x,\text{3D-Gauss}}$ = (190 ± 10) nm, $w_{y,\text{3D-Gauss}}$ = (390 ± 20) nm and $w_{z,\text{3D-Gauss}}$ = (680 ± 10) nm in x-, y- and z-direction, respectively. The conventional three-dimensional Gaussian PSF model and the improved double-cone shaped PSF model are identical in the focal plane, but the improved model function described the shape of the measured PSF in axial direction significantly better (Supplementary Fig. 1a).

Determination of PSF side lobe parameters from msFCCS measurements

For determining the widths, positions and amplitudes of the theoretically expected PSF side lobes, we developed a highly sensitive approach based on multi-scale fluorescence cross-correlation spectroscopy (msFCCS). When determining the PSF from image stacks of fluorescent beads, the background signal consisting of camera readout noise and scattered light has to be accounted for. This is especially relevant for accurately measuring low-amplitude PSF side lobes. The approach presented here intrinsically separates the signal from uncorrelated background noise. It allows for measuring the relevant PSF geometry for FCS model functions, since factors that affect imaging and correlation analysis differently are properly captured. We used single immobilized quantum dots (QDots) as fluctuating point light sources [4]. The emitted fluorescence signals of single QDots were recorded until the QDots switched to a long-lasting non-fluorescent state. Fluorescence signals were analyzed by cross-correlating signals of spatially separated detection volumes. Each curve reflects the QDots' blinking spectrum (Supplementary Fig. 2a,b). To obtain the PSF's structural parameters in the focal plane, we evaluated the fluorescence data as follows: The recorded signal $S_n(t)$ of detection volume n is assumed to contain uncorrelated background

noise $N_n(t)$ and fluctuating fluorescence signal $F_n(t)$ emitted by a single blinking QDot as given by

$$S_n(t) = N_n(t) + F_n(t). \tag{12}$$

Accordingly, the corresponding relative signal fluctuations $\delta S_n(t)$ consist of fluorescence fluctuations $\delta F_n(t)$ and fluctuations due to noise $\delta N_n(t)$

$$\delta S_n(t) = \delta N_n(t) + \delta F_n(t). \tag{13}$$

The noise fluctuations $\delta N_n(t)$ are temporarily uncorrelated, whereas the fluorescence fluctuations $\delta F_n(t)$ are correlated due to QDot blinking. Thus, background noise $N_n(t)$ is removed by correlation of signal fluctuations $\delta S_n(t)$ as shown in Supplementary Eq. 14.

$$\begin{aligned}\langle \delta S(t)\delta S(t+\tau)\rangle &= \langle \delta F(t)\delta F(t+\tau)\rangle + \langle \delta F(t)\delta N(t+\tau)\rangle + \langle \delta N(t)\delta F(t+\tau)\rangle + \langle \delta N(t)\delta N(t+\tau)\rangle \\ &= \langle \delta F(t)\delta F(t+\tau)\rangle\end{aligned}. \tag{14}$$

Fluorescence signals $F_n = \alpha_n F_0$ recorded by each detector pixel n are proportional to the signal emitted by a single QDot with a proportionality coefficient α_n, which gives the PSF's detection efficiency for the corresponding distance d_n from the QDot. The intensity parameter α_n was extracted by cross-correlation of relative signal fluctuations of spatially separated detection volumes according to Supplementary Eq. 15.

$$\langle \delta S_0(t)\delta S_i(t+\tau)\rangle = \alpha_i \langle \delta S_0(t)\delta S_0(t+\tau)\rangle \Rightarrow \alpha_i = \frac{\langle \delta S_0(t)\delta S_i(t+\tau)\rangle}{\langle \delta S_0(t)\delta S_0(t+\tau)\rangle} = \frac{\langle \delta F_0(t)\delta F_i(t+\tau)\rangle}{\langle \delta F_0(t)\delta F_0(t+\tau)\rangle}. \tag{15}$$

The correlation analysis eliminated uncorrelated background noise $N_n(t)$ and thus provided a robust approach for measuring the PSF. Significant PSF amplitudes were measured even for distances larger than 2 µm but positions and widths of the side lobes were difficult to resolve (Supplementary Fig. 2c,d). For determining the side lobe structural parameters and positions, we fitted a theoretical model function [2], which is valid near the focal plane for $x = z = 0$ to the measured PSF data. Furthermore, we approximated PSF lobes of the theoretical model function in the focal plane by asymmetric two-dimensional Gaussian functions. The axial PSF dependence was described as double-cone shape according to Supplementary Eq. 4. The PSF lobe parameters are summarized in Supplementary Table 2.

Computer optimization of PSF structural parameters

The geometry of the PSF double-cones in the *yz*-plane, given by cone angle, curvature of the cone and decrease of the maximum intensity in axial direction, strongly influences the shape of XC curves due to spatially overlapping neighboring detection volumes. To enhance the accuracy of the XC model functions, we further improved the previously measured PSF structural parameters by a computer optimization routine (Supplementary Fig. 3). The optimization is based on the invariance of the measured diffusion coefficients and concentrations with respect to the correlation distance for photo-stable fluorescent particles in water. An additional condition is it that the experimental correlation curves are described well by the model functions. Thus, we fitted XC curves for 0 µm, 1 µm, 2 µm, 3 µm and 4 µm correlation distance of QDots diffusing in aqueous solution with the improved model function and checked for the scale-invariance of the resulting diffusion coefficients and concentrations. The same procedure was repeated for different PSF structural parameter sets. Finally, we selected the parameter set for which the experimental correlation curves were well described by the model functions and additionally the best scale-invariance of the fit results was observed.

The distance between the centers of neighboring detection volumes in the sample was determined via the known distance of the pixels on the EM-CCD camera chip, and the magnification of the optical setup. We determined the magnification of the STFM by a micrometer slide. The resulting detection volume distance in the sample was d = (196 ± 8) nm.

Supplementary Note 3 | Signal correction in Fourier space

Fluorescence signals acquired with the line-confocal microscope in living cells were usually exponentially decaying as a function of time due to photobleaching of fluorescent molecules. An msFCCS measurement is comparable to a parallelized conventional FCS measurement at several hundred positions, leading to significant bleaching of fluorophores mostly in out-of-focus regions. For a quantitative analysis of FCS experiments, the fluorescence signals have to be corrected properly. To this end, different strategies were compared, including correction by a moving average approach or by fitting an exponentially decaying function. Both strategies are well suited for smoothly decaying signals. However, fluorescence signals from measurements in living cells typically contained additional slow fluctuations, e.g. due to movements of large non-fluorescent cellular components through the detection volumes. These fluctuations could only be incompletely corrected by the previously introduced strategies. The resulting correlation artifacts were particularly pronounced in cross-correlation curves for large separation distances, whereas auto-correlation curves were only moderately affected. Therefore, a new approach was developed that allows quantitative analysis of msFCCS measurements in the heterogeneous environment of living cells. This new approach is based on transforming the fluorescence signals $I(t)$ to frequency space by Fourier transformation (FT)

$$\tilde{I}(v) = \mathrm{FT}\left(I(t)\right), \tag{16}$$

and subsequently correcting the low frequency components of the Fourier spectra $\tilde{I}(v)$ to remove slow intensity fluctuations in the time domain:

$$I_{\mathrm{corrected}}(t) = \mathrm{FT}^{-1}\left(\tilde{I}_{\mathrm{corrected}}(v)\right). \tag{17}$$

For correction, spectra from measurements in aqueous solutions were used as a reference and an envelope function was calculated for each spectrum. The envelope function values e_i were determined based on the mean value μ_i and the standard deviation σ_i calculated within a moving window i of twenty data points along the frequency axis:

$$e_i = \mu_i + 3\sigma_i. \tag{18}$$

The envelope of the Fourier spectrum obtained for GFP in aqueous glycerol solution ($\phi = 25\,\%$) was fitted by an empirical model function given by

$$f_{\text{buffer}}(\nu) = a_1 \exp(-k_1\nu) + a_2 \exp(-k_2\nu) + a_3 \exp(-k_3\nu). \quad (19)$$

In this manner, the water envelope parameters a_1, a_2, a_3, k_1, k_2 and k_3 were determined as a reference. An aqueous glycerol solution was used to adjust the diffusion coefficient of GFP to the value measured in living cells. An envelope function $f(\nu)$ proportional to the buffer envelope function $f_{\text{buffer}}(\nu)$ with the parameters determined above was fitted to the Fourier spectra obtained in living cells. The envelope model function with a fit parameter C was defined by Supplementary Eq. 20:

$$f(\nu) = C \cdot f_{\text{buffer}}(\nu). \quad (20)$$

By cropping the high amplitude values at low frequencies of the Fourier spectra according to the fitted buffer envelope function and subsequent back transformation into the time domain, fluorescence signals were corrected prior to correlation analysis (Supplementary Fig. 4).

The Fourier transformation-based approach for signal correction was validated by artificially adding a trend to experimental data obtained from 20 nM QDots in aqueous solution and subsequent correction (Supplementary Fig. 5). After correction, the original auto-correlation curves could be reconstructed without deformations. After correction, the original auto-correlation curves could be reconstructed without deformations. The approach was further validated by correcting the signals of larger and therefore slower TetraSpeck beads with a diffusion coefficient of ~4.4 $\mu m^2 s^{-1}$ [5]. In addition, the approach was tested by correcting measurements of the chromatin-interacting heterochromatin protein 1 (HP1) labeled with green fluorescent protein (GFP) in the nucleus of living cells, which contained slow fluctuations. The mobility of this protein in living cells has been characterized comprehensively in a previous study [6]. A comparison between the moving average approach and the Fourier transformation-based approach is shown in Supplementary Fig. 6. Correlation curves calculated based on fluorescence signals corrected with the moving average approach showed a dip at the time of half the window size and correlations above this time scale were removed (Supplementary Fig. 6c). Thus, the Fourier transformation based correction is better suited for msFCCS analysis since the measured translocation times are longer and the relevant information is present on larger time scales in spatial cross-correlation curves compared to auto-correlation curves.

Supplementary Note 4 | Correlation function for the improved PSF model

The shape of the correlation curves is determined by the microscope's PSF, photophysical properties of fluorescent dyes and transport processes like diffusion or directed flow that result in the detected intensity fluctuations of the fluorescence signal. To account for the properties of the crowded interior of living cells we used an anomalous diffusion propagator with a power law relation for the molecules' mean squared displacement (MSD). However, we made our final results model-independent by calculating the effective translocation time t_{eff} for the translocation of molecules from detection volume *k to* detection volume *l*. The propagator used here reads

$$P_{\mathrm{D}}\left(\mathbf{r}_2,\tau \mid \mathbf{r}_1,0\right)=\frac{1}{\left(4\pi\Gamma\tau^{\alpha}\right)^{3/2}}\exp\left(-\frac{\left(\mathbf{r}_2-\mathbf{r}_1\right)^2}{4\Gamma\tau^{\alpha}}\right). \tag{21}$$

With the improved PSF model function (Supplementary Eq. 3) and the propagator (Supplementary Eq. 21) we derived a model function $G_{kl}(\tau)$ given by Supplementary Eq. 22 for quantitative description of correlation curves obtained by correlating fluorescence signals acquired from detection volumes *k* and *l*:

$$G_{kl}(\tau)=\frac{\int_V\int_V \Psi_k\left(\mathbf{r}_1\right)P_D\left(\mathbf{r}_1,0\mid\mathbf{r}_2,\tau\right)\Psi_l\left(\mathbf{r}_2\right)d^3r_1d^3r_2}{\int_V\Psi_k(\mathbf{r}_1)d^3r_1\int_V\Psi_l(\mathbf{r}_2)d^3r_2}=\frac{1}{cV_{\text{eff}}}\sum_{m=-4}^{4}\sum_{n=-4}^{4}H_{klmn}(\tau). \tag{22}$$

For $k = l$ the auto-correlation (AC) curve is obtained, while $k \neq l$ yields a spatial cross-correlation (XC) curve. $N = cV_{\text{eff}}$ gives the mean number of particles in the focus volume. The effective volume was calculated by

$$V_{\text{eff}}=\int_V\Psi(\mathbf{r})d^3r=\frac{\pi}{2}\sum_{n=-4}^{4}A_n w_{x,n}(0)w_{y,n}(0)\int_{-\infty}^{\infty}\kappa(z)dz. \tag{23}$$

The function $H_{klmn}(\tau)$ in Supplementary Eq. 22 is defined by Supplementary Eq. 24 and gives the probability that a particle is detected at time $t = 0$ in lobe *m* of detection volume *k* and at time $t = \tau$ in lobe *n* of detection volume *l*.

$$H_{klmn}(\tau)=\frac{A_mA_n}{2V_{\text{eff}}}w_{x,m}(0)w_{y,m}(0)w_{x,n}(0)w_{y,n}(0)h_{klmn}(\tau). \tag{24}$$

The function $h_{klmn}(\tau)$ is given by

$$h_{klmn}(\tau) = \sqrt{\frac{\pi}{4\Gamma\tau^{\alpha}}} \int_{-\infty}^{\infty} \int_{-\infty}^{\infty} \zeta_{klmn}(z_1, z_2, \tau) dz_1 dz_2 \,. \tag{25}$$

The expression $\zeta_{klmn}(z_1,z_2,\tau)dz_1dz_2$ in Supplementary Eq. 25 gives the probability for molecules to be detected at time $t = 0$ in a dz_1 thick cross-section through lobe m around the axial position z_1 and at time $t = \tau$ in a dz_2 thick cross-section through lobe n at position z_2 and vice versa. $\zeta_{klmn}(z_1,z_2,\tau)$ is given by

$$\zeta_{klmn}(z_1, z_2, \tau) = \frac{\kappa(z_1)\kappa(z_2)}{\sqrt{f_{mn,x}(z_1, z_2, \tau)}\sqrt{f_{mn,y}(z_1, z_2, \tau)}} \exp\left(-\frac{(z_2 - z_1)^2}{4\Gamma\tau^{\alpha}} - 2\frac{\Delta_{klmn}^2(z_1, z_2)}{f_{mn,y}(z_1, z_2, \tau)} \right). \tag{26}$$

Here, the functions $\Delta_{klmn}(z_1, z_2)$ and $f_{mn,i}(z_1, z_2, \tau)$ with $i = x, y$ are given by Supplementary Eq. 27 and 28, respectively:

$$\Delta_{klmn}(z_1, z_2) = y_m(z_1) - (d_{kl} + y_n(z_2)) \,, \tag{27}$$

$$f_{mn,i}(z_1, z_2, \tau) = w_{i,m}^2(z_1) + w_{i,n}^2(z_2) + 8\Gamma\tau^{\alpha}. \tag{28}$$

All correlation curves were fitted by a least squares fitting routine of the GNU Scientific Library (GSL) with the nonlinear model function described above [7].

Supplementary Note 5 | Fluorescence recovery after photo-bleaching analysis of GFP multimers

Fluorescence recovery after photobleaching (FRAP) measurements were used to measure the percentage of trapped GFP multimers in the cytoplasm and nucleus of U2OS cells. FRAP experiments were conducted using a Leica SP5 microscope equipped with an HCX PL APO lambda blue 63x oil immersion objective. Images were acquired with 128x128 pixels at 1,400 Hz, which corresponds to a frame acquisition time of roughly 100 ms. Circular bleach regions with a nominal radius of 1.0 µm were selected. For simultaneously bleaching GFP and RFP molecules, an argon laser at 488 nm and a diode-pumped solid-state laser at 561 nm with a power of roughly 2 mW in the back focal plane were used. FRAP data were analyzed with a recently published model that accounts for partial fluorescence recovery during the bleach process [8]. For this purpose, the bleach depth K_M and the width w_M of the radial intensity profiles in the first post-bleach image frame were determined (Supplementary Table 4) by fitting a model function to the normalized profiles (Eq. 29). Appropriate description of the bleach profile has been shown to be critical for robust analysis of the recovery curve [9]. Since we observed immobile fluorescent molecules as a "step" in the radial intensity profiles at a radial distance w_b = 1.3 µm from the center of the circular bleach region, we modified the model function $F_M(r)$ from ref. [8] with a term that accounts for a trapped fraction $f_{\mathrm{trap}}^{100\,\mathrm{ms}}$ on the 100 ms time-scale corresponding to the frame acquisition time:

$$F(r) = F_0\left[\exp\left(-K_{\mathrm{M}}\exp\left(-2\frac{r^2}{w_{\mathrm{M}}^2}\right)\right) - f_{\mathrm{trap}}^{100\,\mathrm{ms}}\left(1-\Theta\left(r-w_{\mathrm{b}}\right)\right)\right]. \tag{29}$$

Thus, the time course of the averaged fluorescence intensity of the bleach region with the measured radial profile width w_M is given by

$$F(t) = F_0\left[\frac{1-f_{\mathrm{trap}}^{1\,\mathrm{min}}}{2}\left(\frac{w_{\mathrm{M}}^2}{w_{\mathrm{b}}^2}\left[\sum_{n=1}^{\infty}\frac{\left(-K_{\mathrm{M}}\right)^n}{n!\,n}\left(1-\exp\left(-2\frac{n}{1+2nt/\tau_D}\frac{w_{\mathrm{b}}^2}{w_{\mathrm{M}}^2}\right)\right)\right]+2\right)\right]. \tag{30}$$

From a fit of the data to Supplementary Eq. 30 the bleach depth K_M, the trapped fraction $f_{\mathrm{trap}}^{1\,\mathrm{min}}$ on the minute time-scale and the diffusion coefficient $D = w_{\mathrm{M}}^2/\left(4\tau_{\mathrm{D}}\right)$ were determined (Supplementary Table 4).

Supplementary Note 6 | Effective translocation distance and time

The mean distance molecules diffuse if they are consecutively detected in detection volumes Ψ_k and Ψ_l depends on the detection volume geometry and the separation distance between the centers of the detection volumes. For large separation distances, the actual size and geometry of the volumes becomes negligible. The mean effective translocation distance $\langle d_{kl} \rangle$ between two detection volumes *k* and *l* is the characteristic length scale for the measurement. It can be calculated as the average distance between all combinations of two points in the different volumes weighted with the corresponding detection efficiencies given by the PSF. Due to the spatial extension of the PSF, $\langle d_{kl} \rangle$ is larger than the distance Δ between the centers of the respective detection volumes. Thus, $\langle d_{kl} \rangle$ was calculated according to

$$\left\langle d_{kl} \right\rangle = \frac{\int \psi_{0,k}\left(x_1,y_1,0\right)\left|\mathbf{r}_2 - \mathbf{r}_1\right|_{z=0} \psi_{0,l}\left(x_2,y_2,0\right) dx_1 dy_1 dx_2 dy_2}{\int \psi_{0,k}\left(x_1,y_1,0\right) dx_1 dy_1 \int \psi_{0,l}\left(x_2,y_2,0\right) dx_2 dy_2}. \tag{31}$$

For simplicity, the PSF in Eq. 31 was approximated by its main lobe. To determine the effective translocation time, we fitted the model function in Supplementary Eq. 22 to the measured cross-correlation curves. The effective translocation time $\langle t_{kl} \rangle$ for the translocation of molecules between detection volumes *k* and *l* can be calculated based on the resulting fit parameters, i.e. transport coefficient Γ and anomaly parameter α:

$$\left\langle t_{kl} \right\rangle = \left(\left\langle d_{kl} \right\rangle^2 / (6\Gamma) \right)^{1/\alpha}. \tag{32}$$

The effective translocation time is a good measure for characterizing the scaling behavior of transport processes, since it is rather independent of the specific propagator used for fitting the correlation curves. This is due to the fact that the maximum amplitude of the correlation curve determines the effective translocation time, which is rather robustly obtained from spatial XC curves for large separation distances even without fitting a particular model function. The diffusion coefficient *D* was calculated from the effective translocation time and translocation distance according to

$$D_{\text{app}} = \frac{\left\langle d_{kl} \right\rangle^2}{6\left\langle t_{kl} \right\rangle}. \tag{33}$$

Supplementary Note 7 | Estimation of occupied volume fraction and obstacle size

The retardation of the particle *R* is defined here as the ratio of microscopic diffusion coefficient D_0 and macroscopic diffusion coefficient D_∞. It was measured as a function of the molecular weight *M* of GFP_1, GFP_3 and GFP_5 in nucleus and cytoplasm. The retardation values were fitted by a hydrodynamic model function for hindered diffusion in an environment of randomly placed fibrous obstacles, which does not rely on an effective medium approximation [1]. In this model, the volume fraction Φ_0 occupied by fibrous obstacles and their radius r_{fiber} characterize the random fiber network. Supplementary Eq. 34 gives the inverse retardation $1/R$ as a function of the tracer radius r_{tracer}:

$$\frac{1}{R} = F\left(\lambda_{\mathrm{P}},\Phi_0\right) S\left(\lambda_{\mathrm{P}},\Phi_0\right). \tag{34}$$

Here, $\lambda_{\mathrm{P}} = r_{\mathrm{fiber}}/r_{\mathrm{tracer}}$ is the ratio of the fiber radius and the tracer radius. The term $F\left(\lambda_{\mathrm{p}},\Phi_0\right)$ in Supplementary Eq. 34 is defined in Supplementary Eq. 35 and accounts for hydrodynamic effects.

$$F\left(\lambda_{\mathrm{P}},\Phi_0\right) = \exp\left(-a\left(\lambda_{\mathrm{P}}\right)\Phi_0^{b\left(\lambda_{\mathrm{P}}\right)}\right). \tag{35}$$

Further, the term $S\left(\lambda_{\mathrm{P}},\Phi_0\right)$ in Supplementary Eq. 34 accounts for steric or tortuosity effects:

$$S\left(\lambda_{\mathrm{P}},\Phi_0\right) = \exp\left(-0.84 \cdot f\left(\lambda_{\mathrm{P}},\Phi_0\right)^{1.09}\right), \tag{36}$$

with an adjusted volume fraction that reads as follows

$$f\left(\lambda_{\mathrm{P}},\Phi_0\right) = \left(1+\frac{1}{\lambda_{\mathrm{P}}}\right)^2 \Phi_0. \tag{37}$$

This model is applicable for small and moderate obstacle concentrations since in this regime the mobility constraints imposed by a polymer network or a random obstacle distribution are similar [10]. The fit parameters are the volume fraction occupied by obstacles Φ_0 and the radius of the fibers r_{fiber}. For the relation between molecular weight *M* and effective hydrodynamic radius we used the expression in Pack et al. [11] for ellipsoidal molecules with a

rigid α-helical shaped linker between neighboring GFP molecules. The effective hydrodynamic radius of monomeric GFP was calculated according to the Stokes-Einstein relation for the measured diffusion coefficient D_{GFP} = (88 ± 3) μm^2 s^{-1} in aqueous solution at temperature T = (295 ± 1) K as r_{GFP} = (2.8 ± 0.1) nm. The value for the diffusion coefficient of GFP in aqueous solution agreed well with results from scanning FCS measurements [12]. The hydrodynamic radii for GFP_3 und GFP_5 were calculated as 5.5 nm and 7.9 nm, respectively. To fit Supplementary Eq. 34, the polynomial interpolation for the hindered diffusion parameters *a* and *b* as functions of the ratio $\lambda_P = r_{fiber}/r_{tracer}$ reported in [1] was replaced by an exponential interpolation (Supplementary Fig. 8). This approximation yielded a similar fit quality as the polynomial approximation but avoided diverging *a* and negative *b* parameters for λ_p values that were larger than the ones included in [1]. This is advantageous for the fitting process and allowed for moderate extrapolation to larger λ_p values.

Supplementary References

1. Phillips RJ. A hydrodynamic model for hindered diffusion of proteins and micelles in hydrogels. *Biophys J* **79**, 3350-3353 (2000).
2. Dusch E, Dorval T, Vincent N, Wachsmuth M, Genovesio A. Three-dimensional point spread function model for line-scanning confocal microscope with high-aperture objective. *J Microsc* **228**, 132-138 (2007).
3. Dertinger T, Pacheco V, von der Hocht I, Hartmann R, Gregor I, Enderlein J. Two-focus fluorescence correlation spectroscopy: a new tool for accurate and absolute diffusion measurements. *Chemphyschem* **8**, 433-443 (2007).
4. Nirmal M*, et al.* Fluorescence intermittency in single cadmium selenide nanocrystals. *Nature* **383**, 802-804 (1996).
5. Muller CB*, et al.* Precise measurement of diffusion by multi-color dual-focus fluorescence correlation spectroscopy. *Europhys Lett* **83**, 46001 (2008).
6. Müller KP*, et al.* Multiscale analysis of dynamics and interactions of heterochromatin protein 1 by fluorescence fluctuation microscopy. *Biophys J* **97**, 2876-2885 (2009).
7. Galassi M*, et al. Gnu Scientific Library: Reference Manual*. Network Theory Ltd. (2003).
8. Braga J, Desterro JM, Carmo-Fonseca M. Intracellular macromolecular mobility measured by fluorescence recovery after photobleaching with confocal laser scanning microscopes. *Mol Biol Cell* **15**, 4749-4760 (2004).
9. Mueller F, Wach P, McNally JG. Evidence for a common mode of transcription factor interaction with chromatin as revealed by improved quantitative fluorescence recovery after photobleaching. *Biophys J* **94**, 3323-3339 (2008).
10. Fritsch CC, Langowski J. Anomalous diffusion in the interphase cell nucleus: the effect of spatial correlations of chromatin. *J Chem Phys* **133**, 025101 (2010).
11. Pack C, Saito K, Tamura M, Kinjo M. Microenvironment and effect of energy depletion in the nucleus analyzed by mobility of multiple oligomeric EGFPs. *Biophys J* **91**, 3921-3936 (2006).
12. Petrasek Z, Schwille P. Precise measurement of diffusion coefficients using scanning fluorescence correlation spectroscopy. *Biophys J* **94**, 1437-1448 (2008).